Advanced activation of persulfate by polymeric g-C3N4 based photocatalysts for environmental remediation: A review

Vasudha Hasija, Van-Huy Nguyen, Ajay Kumar, Pankaj Raizada, Venkata Krishnan, Aftab Aslam Parwaz Khan, Pardeep Singh, Eric Lichtfouse, Chuanyi Wang, Pham Thi Huong

To cite this version:

Vasudha Hasija, Van-Huy Nguyen, Ajay Kumar, Pankaj Raizada, Venkata Krishnan, et al.. Advanced activation of persulfate by polymeric g-C3N4 based photocatalysts for environmental remediation: A review. Journal of Hazardous Materials, 2021, 413, pp.1-14. 10.1016/j.jhazmat.2021.125324 . hal-03139576

HAL Id: hal-03139576
https://hal.science/hal-03139576

Submitted on 12 Feb 2021

Journal of Hazardous Materials 413 (2021) 125324
https://doi.org/10.1016/j.jhazmat.2021.125324

Review

Advanced activation of persulfate by polymeric g-C_3N_4 based photocatalysts for environmental remediation: A review

Vasudha Hasija [a], Van-Huy Nguyen [b], Ajay Kumar [c], Pankaj Raizada [a], Venkata Krishnan [c], Aftab Aslam Parwaz Khan [d,e], Pardeep Singh [a,*], Eric Lichtfouse [f,g,1], Chuanyi Wang [h], Pham Thi Huong [i,j]

[a] *School of Advanced Chemical Sciences, Shoolini University, Solan, Himachal Pradesh 173229, India*
[b] *Key Laboratory of Advanced Materials for Energy and Environmental Applications, Lac Hong University, Dong Nai 810000, Viet Nam*
[c] *School of Basic Sciences and Advanced Materials Research Center, Indian Institute of Technology Mandi, Kamand, Mandi 175075, Himachal Pradesh, India*
[d] *Center of Excellence for Advanced Materials Research, King Abdulaziz University, P.O.Box 80203, Jeddah 21589, Saudi Arabia*
[e] *Chemistry Department, Faculty of Science, King Abdulaziz University, P.O.Box 80203, Jeddah, Saudi Arabia*
[f] *Aix-Marseille Univ, CNRS, IRD, INRA, Coll France, CEREGE, Aix-en-Provence 13100, France*
[g] *International Research Centre for Renewable Energy, State Key Laboratory of Multiphase Flow in Power Engineering, Xi'an Jiaotong University, Xi'an, PR China*
[h] *School of Environmental Science and Engineering, Shaanxi University of Science and Technology, Xi'an 710021, PR China*
[i] *Institute of Research and Development, Duy Tan University, Da Nang 550000, Viet Nam*
[j] *Faculty of Environment and Chemical Engineering, Duy Tan University, Da Nang 550000, Viet Nam*

ABSTRACT

Photocatalytic materials for photocatalysis is recently proposed as a promising strategy to address environmental remediation. Metal-free graphitic carbon nitride (g-C_3N_4), is an emerging photocatalyst in sulfate radical based advanced oxidation processes. The solar-driven electronic excitations in g-C_3N_4 are capable of peroxo (O–O) bond dissociation in peroxymonosulfate/peroxydisulfate (PMS/PDS) and oxidants to generate reactive free radicals, namely $SO_4^{\bullet-}$ and $OH^{\bullet}$ in addition to $O_2^{\bullet-}$ radical. The synergistic mechanism of g-C_3N_4 mediated PMS/PDS photocatalytic activation, could ensure the generation of $OH^{\bullet}$ radicals to overcome the low reductive potential of g-C_3N_4 and fastens the degradation reaction rate. This article reviews recent work on heterojunction formation (type-II heterojunction and direct Z-scheme) to achieve the bandgap for extended visible light absorption and improved charge carrier separation for efficient photocatalytic efficiency. Focus is placed on the fundamental mechanistic routes followed for PMS/PDS photocatalytic activation over g-C_3N_4-based photocatalysts. A particular emphasis is given to the factors influencing the PMS/PDS photocatalytic activation mechanism and the contribution of $SO_4^{\bullet-}$ and $OH^{\bullet}$ radicals that are not thoroughly investigated and require further studies. Concluding perspectives on the challenges and opportunities to design highly efficient persulfate-activated g-C_3N_4 based photocatalysts toward environmental remediation are also intensively highlighted.

Keywords:
PMS/PDS photocatalytic activation
$SO_4^{\bullet-}$ generation
Graphitic carbon nitride
Photocatalysis
Heterojunction
Environmental remediation

1. Introduction

To date, industrialization and a rapidly expanding population result in many discharges of effluents into water bodies. In typical, the emerging industrial organic contaminants are toxic and non-biodegradable, for example, synthetic dyes, personal health care products, pharmaceuticals, illicit drugs, endocrine disruptors, etc. (Mamba and Mishra, 2016; Hasija et al., 2018). This result leads to pernicious effects on aquatic, anthropogenic flora units and further multiplies the water scarcity problem. It has become essential to develop renewable, efficient, and cheap wastewater treatment technologies to resolve the global issue of useable water (Yi et al., 2018; Sudhaik et al., 2018; Kumar et al., 2021; Hasija et al., 2020; Dominguez and Gujer, 2006; Nguyen et al., 2020). The most beneficial advancement is advanced oxidation processes (Miklos et al., 2018), such as ozone and ozone-hybrid based processes (O_3, O_3/H_2O_2, O_3/H_2O_2/UV) (Valerio et al., 2020; Agustina et al., 2005), Fenton (H_2O_2/Fe^{2+}) (Brillas, 2020), and photo-Fenton reaction (Fe^{2+}/H_2O_2/UV) (Brillas and Segura, 2020),

---

* Corresponding author.
E-mail address: pardeepsingh@shooliniuniversity.com (P. Singh).
[1] ORCID ID: 0000-0002-8535-8073

sono-photochemical oxidation (Reddy et al., 2003) and photocatalysis for the degradation of toxic pollutants into harmless mineralized salts, H_2O and CO_2 via highly reactive free radicals. The hydroxyl ($OH^{\bullet}$) radical is the most widely used reactive oxidative species possessing 2.8 V oxidation potential that reacts non-selectively with toxic organic molecules (Patial et al., 2020; Singh et al., 2019). Despite its powerful oxidation ability, $OH^{\bullet}$ based advanced oxidation processes have faced significant restrictions of instability, limited degradation potential for carbonate/bicarbonate ions, and pH-dependence (acidic environment) is required for effective generation of $OH^{\bullet}$ radicals (Dutta et al., 2019; Chandel et al., 2019). It is desirable to seek a more potent oxidant than $OH^{\bullet}$ radical to enhance oxidative degradation ability for contaminants removal. Table S1 demonstrates the redox potential of common chemical oxidants (Bard et al., 1985; Wardman, 1989; Chen et al., 2018). Recently, sulphate radicals ($SO_4^{\bullet-}$) based advanced oxidation processes have successfully replaced $OH^{\bullet}$ based advanced oxidation processes to a certain extent (Hu et al., 2020; Xiao et al., 2019; Oh et al., 2016). The generation of $SO_4^{\bullet-}$ is typically from reactive oxidants, i.e., peroxydisulfate (PDS, $S_2O_8^{2-}$) and peroxymonosulfate (PMS, HSO_5^-). The fundamental explanation of PDS/PMS is provided in [S-1.1]. The following factors promote the PDS as a preferred oxidant:

- Higher potential of PDS (E° ($S_2O_8^{-2}/SO_4^{-2}$) = 2.01 V_{NHE} that of PMS (E° (HSO_5^-/SO_4^{-2}) = 1.75 V_{NHE} (Matzek and Carter, 2016).
- The low cost of PDS i.e.; 0.18 USD/mol whereas, 1.36 USD/mol for PMS (Duan et al., 2015).
- The half-life ($t_{1/2}$) of PDS is five months, and PMS has $t_{½}$ of hours to a few days (Ghanbari and Moradi, 2017).
- The longer O–O bond distance of PDS (1.497 Å) compared to PMS (1.460 Å) requires lesser bond energy for O–O bond fission in PDS (Lee et al., 2020b).

Although PMS and PDS are potential oxidizers for recalcitrant mineralization of pollutants, they operate at a slow reaction rate. Hence the activation of PMS/PDS is required, which mainly occurs via external energy exposure, including heat (Yang et al., 2010), ultrasound (Yin et al., 2018) and ultraviolet (UV) (Fang and Shang, 2012), gamma irradiations (Chan and Chu, 2009), transition metal (Fe, Mn, Cu, Co, etc.) based homogenous and heterogeneous catalytic oxidation (Rojas et al., 2020) and photocatalytic activation (Yu et al., 2020).

These processes illustrated in Fig. 1 can activate PMS/PDS; however, the limitations listed below:

- Heat and ultrasound-driven PMS/PDS activation require expensive reactors, which hinders its large-scale applicability.
- UV-rays have less penetration power in water and destructive O–O bond in PMS/PDS only up to 254 nm.
- Direct visible light has a low photon energy of 1.63–3.26 eV, which is insufficient to activate PMS/PDS directly.
- Exposure to gamma radiations is a cost-ineffective process resulting in $OH^{\bullet}$, hydrogen atoms, and hydrated electrons, which undergo side-chain reactions.
- Transition metal ions mediated catalytic oxidation is highly dependent on the pH of the water matrix, i.e., they precipitate at the basic conditions and undergo hydration in an acidic medium. Also, there are several limitations to metal-based photocatalytic systems. The prime concern is the recovery of metal ions due to low recyclability and resource unavailability (Wang et al., 2020b). Secondly, a higher concentration of metal-based photocatalyst is required for the degradation of high amounts of pollutants, which results in the presence of metal ions in the effluent. The excessive amount of metal ions leads to unwanted reactions with organic pollutants affecting PMS/PDS activation (Ye et al., 2018). Another unwanted

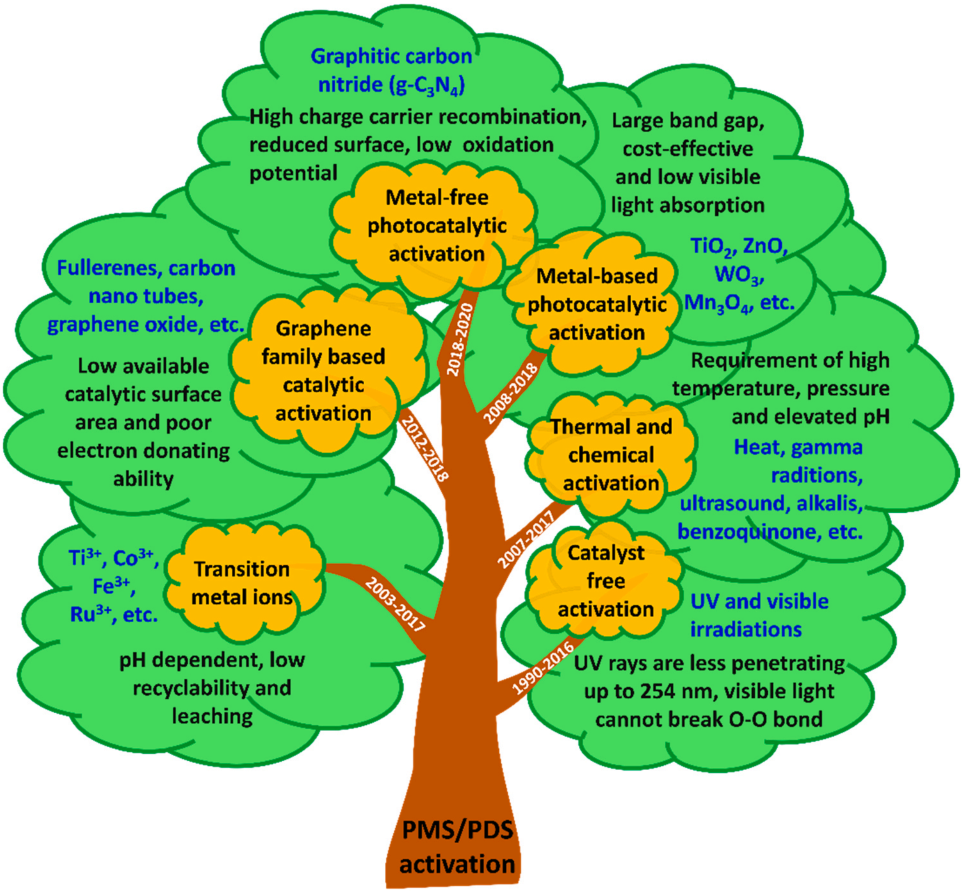

Fig. 1. Evolution tree of peroxymonosulfate/peroxydisulfate (PMS/PDS) activation methods with their respective disadvantages.

phenomenon is metal leaching, which causes biotoxicity and inhibits the effective generation of reactive oxidative species from PMS/PDS precursor salts. Thirdly, metal ions precipitate at higher pH and hydrates under acidic conditions, decreasing activation ability (Hu et al., 2017). The drawbacks of traditional PMS/PDS activation methods are overcome by solar irradiation driven semiconductor-based photocatalysis. The advancements in photocatalysis have allowed an extension from UV to visible light utilization. Therefore, organic pollutant elimination via PMS/PDS photocatalytic activation has become more energy efficient.

The metal-free carbonaceous catalysts have successfully gauged PMS/PDS activation's true potential due to inherent properties of abundant availability, tunable structure, absorption in the extended solar spectrum, and extremely stable nature. The high solar energy absorption efficiency and lack of secondary pollution make them eco-friendly. Nevertheless, metal-free photocatalysts have drawbacks of low stability, poor separability, and inefficient visible light activity. A typical structural representation of all the metal-free carbonaceous catalysts has been illustrated in Fig. 2a. They have been classified depending on the variation in active-sites and carbon arrangement as 0D (C_{60} and nano-diamond) (Zhou et al., 2020), 1D (carbon nanotubes) (Liu et al., 2020a), 2D (graphene, graphene oxide, reduced graphene oxide, graphitic carbon nitride (g-C_3N_4)) (Wang and Wang, 2018) and 3D ordered mesoporous carbon like (activated carbon, carbon fiber, and biochar) (Li et al., 2020). As presented in Fig. 2b, metal-free carbonaceous catalysts transfer electrons for O-O bond cleavage in PMS/PDS following either radical or non-radical pathway. The non-radical catalytic oxidation process over metal-free carbonaceous catalysts follows either of the three dominant reaction pathways, as explained in [S-1.2]. Identifying specific active sites in metal-free carbonaceous catalysts participating in PMS/PDS activation has been the vital element of research to determine the precise oxidative degradation mechanism of pollutants (Wang et al., 2020a). Compared to traditional non-photocatalytic processes, the visible light-assisted g-C_3N_4 generates $O_2^{\bullet -}$ and holes (Cao et al., 2015). However, the inability to generate OH^- can be overcome by coupling g-C_3N_4 with PMS/PDS oxidants assisted by photocatalysis technology (Xiao et al., 2018). The essence of a π-conjugated g-C_3N_4-based photocatalyst depends on the irradiated electrons in the conduction band, which causes a reduction of PMS/PDS (electron acceptors) for the release of reactive oxidative species (Dong et al., 2014). Typically, the photocatalysis in g-C_3N_4 encompasses the release of three primary free radicals, i.e., $SO_4^{\bullet -}$, $OH^{\bullet}$, and $O_2^{\bullet -}$ with higher oxidative potential, which serves as electron acceptors to oxidize organic pollutants (Qi et al., 2020).

The Scopus database literature survey revealed a progression in 2D g-C_3N_4 photocatalysts as a metal-free alternative for effectual PMS/PDS photocatalytic activation over the last 10 years, as presented in Fig. 3. This observation indicates a considerable interest in exploring g-C_3N_4-based heterostructures for photocatalytic PMS/PDS activation. Although few reviews have addressed graphene (Ma et al., 2020; Wang et al., 2017b), reduced graphene oxide, and g-C_3N_4 for water splitting

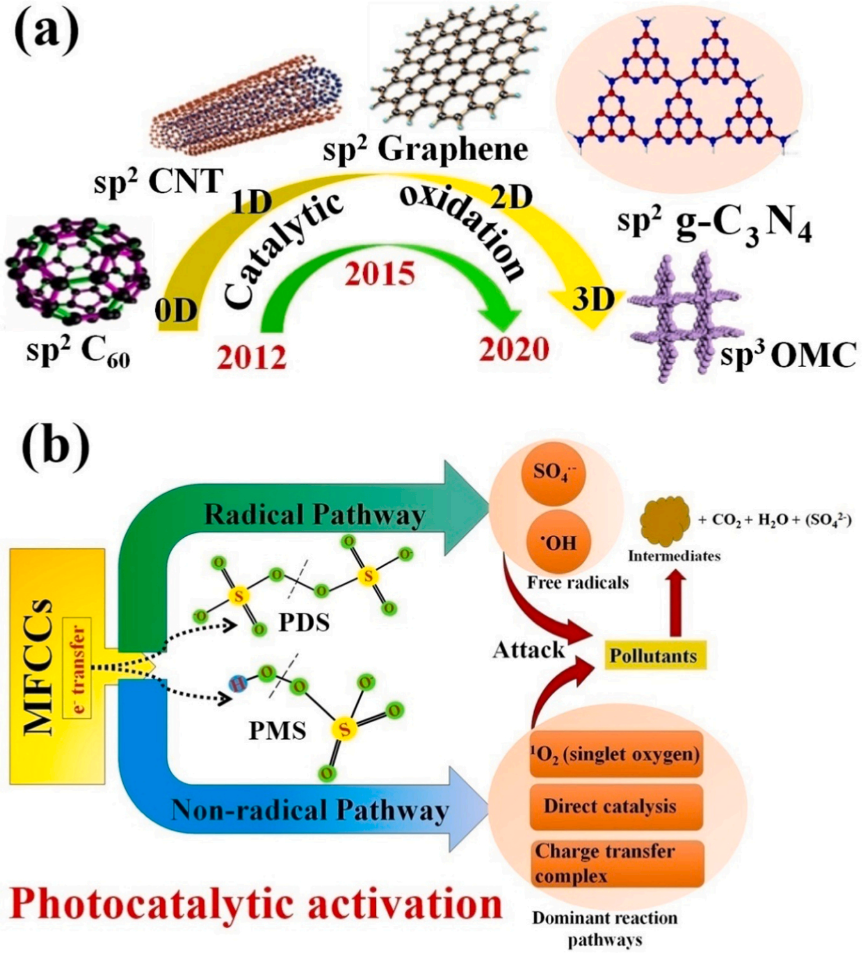

Fig. 2. (a) Development of metal-free carbon catalysts, i.e., fullerenes (C60), carbon nanotubes (CNTs), graphene, graphitic carbon nitride (g-C_3N_4), ordered mesoporous carbon (OMC) in PMS/PDS advanced oxidation processes, and (b) scheme of PMS/PDS activation via radical and non-radical pathway for pollutant degradation.

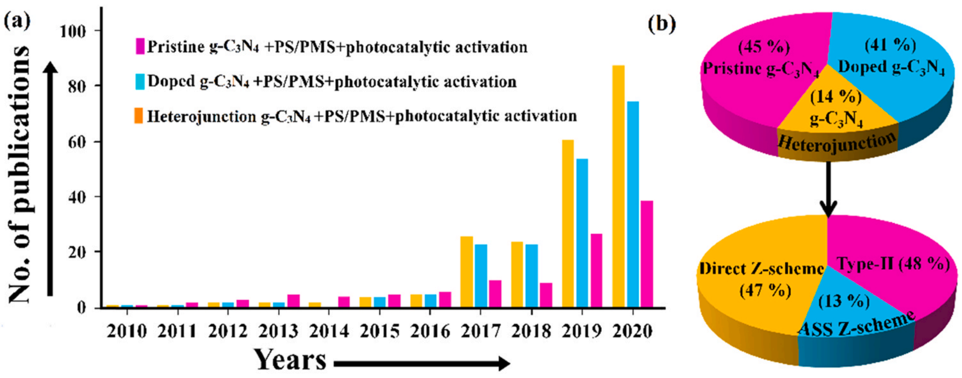

Fig. 3. Bar graph and pie chart representing list of publications from Scopus data base on photocatalytic peroxymonosulfate/peroxydisulfate activation (PMS/PDS) via graphitic carbon nitride (g-C_3N_4) in the years 2010- August 2020 using the keywords; (a) pristine g-C_3N_4 + PMS/PDS + photocatalytic activation, doped g-C_3N_4 + PMS/PDS + photocatalytic activation, heterojunction g-C_3N_4 + PMS/PDS+ photocatalytic activation and (b) type-II heterojunction + g-C_3N_4 + PMS/PDS + photocatalytic activation, all-solid-state Z-scheme + PMS/PDS + photocatalytic activation, direct Z-scheme heterojunction g-C_3N_4 + PMS/PDS + photocatalytic activation.

(Yi et al., 2020), adsorption (Fronczak, 2020), and photocatalytic oxidation of pollutants via PDS activation (Jiang et al., 2016). However, none has put together photocatalytic PDS and PMS activation via g-C_3N_4 targeted for organic pollutant elimination. The review aims to evaluate g-C_3N_4 potential abilities for photocatalytic PMS/PDS activation and the strategies to address the research gap on $SO_4^{\bullet-}$ driven photodegradation mechanisms.

This review begins with the current water pollution status and an overview of conventional water remediation techniques. We present a concise account of the benefits of $SO_4^{\bullet-}$ based advanced oxidation processes over $OH^{\bullet}$ radical driven processes and PDS and PMS activation advantages via photocatalysis over other activation methods. Diagrammatic illustrations on the basics of PMS/PDS photocatalytic activation mechanism and perks of emerging 2D metal-free carbonaceous photocatalysts form part of the introduction section. The other section of the review exemplifies the tailoring of g-C_3N_4 via heterojunction formation to enhance the PDS and PMS photocatalytic activation. Specifically, the development of heterostructure formation accompanying g-C_3N_4, i.e., type-II and Z-scheme charge transfer routes, is elaborated to depict superior dissociation and optimal radiated charge carriers

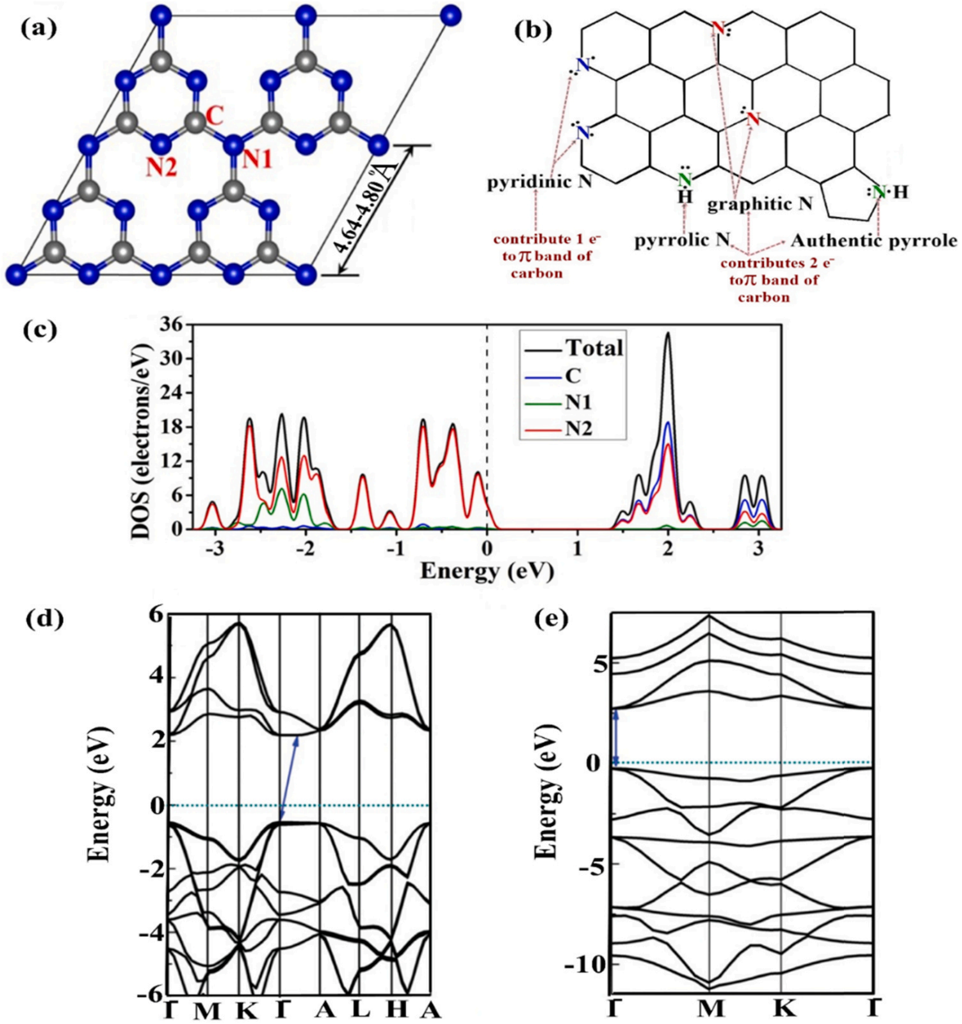

Fig. 4. (a) Geometric structural monolayer of s-triazine based graphitic carbon nitride; g-C_3N_4, carbon and nitrogen atoms are shown by grey and blue spheres, respectively, (b) available electron donating sites in g-C_3N_4 lattice, (c) density of states of g-C_3N_4, (d) calculated band constructions of bulk g-C_3N_4 and monolayer g-C_3N_4. (For interpretation of the references to colour in this figure legend, the reader is referred to the web version of this article.) Reprinted with permission from Refs. Zhu et al. (2019) and Liu et al. (2016).

availability for PMS/PDS photocatalytic activation process. The effect of influential parameters, including increment in specific surface area, the effect of pH, and PMS/PDS concentration, are commendably assessed. The conclusive remarks and future perspectives are proposed to improve the PMS/PDS photocatalytic activation mechanism for its industrial-scale applicability in organic pollutant abatement.

2. PMS/PDS photoactivation using graphitic carbon nitride (g-C_3N_4)

The primarily intended goal of PMS/PDS photocatalytic activation is the release of large amounts of $SO_4^{\bullet-}$ and $OH^{\bullet}$ radicals, which is achieved in the g-C_3N_4 framework due to its structural and inherent properties. The density functional theory (DFT) investigation on g-C_3N_4 has theoretically identified its structure as s-triazine based on C and N atomic arrangement, as shown in Fig. 4a. The N atoms at three coordinated (N1) and two-coordinated (N2) triazine units serve as electron-donating sites for peroxide bond cleavage, as shown in Fig. 4b. The density of states studies calculated via generalized gradient approximation (GGA)-PBE functional theory manifests valence band of g-C_3N_4 composed of N2 atoms and conduction band with N_2, C atoms, as illustrated in Fig. 4c (Zhu et al., 2019). The theoretical bandgap results of monolayer g-C_3N_4 exhibit a larger bandgap (2.93 eV) than bulk g-C_3N_4 (2.73 eV) due to the quantum confinement effect as obtained by the Heyd-Scuseria-Ernzerhof (HSE06) hybrid functional method, as presented in Fig. 4d, and e (Liu et al., 2016). The well-configured optical band alignment of 2.7 eV corresponding to an optical wavelength of 460 nm makes it active in the extended solar spectrum (Raizada et al., 2019c, 2020; Zhu et al., 2014). As a novel metal-free conjugated polymeric semiconductor, g-C_3N_4 is quite different from other metal-free carbonaceous catalysts due to its inherent advantages, such as being earth-abundant thermal and chemical stability and visible-light responsiveness nature, as well as the tuneable morphology (Raizada et al., 2019a; Sano et al., 2019). The PMS/PDS photocatalytic activation on g-C_3N_4 involves electronic transitions of electrons from valence band (1.4 eV) to − 1.3 eV potential in conduction band, leaving holes in valence band, and subsequently leading to the formation of reactive oxidative species for pollutant mineralization as explained in the following discussion.

The large number of photogenerated electrons in the conduction band of g-C_3N_4 contributes to the photocatalytic activation of PDS (Lee et al., 2020a). For instance, the synergistic photocatalytic mechanism between PDS and mesoporous g-C_3N_4, as shown in Fig. 5a, confirmed the photoinduced electrons in photocatalytic activation of $S_2O_8^{2-}$ for facile generation of $SO_4^{\bullet-}$, $OH^{\bullet}$ radicals. The photodegradation results in PDS/m-g-C_3N_4 revealed 99% elimination of β-lactam antibiotics, i.e., amoxicillin, cefotaxime, meropenem within 60 min of visible light irradiations at pH 7.0; however, only 10% of sulbactam was removed. In bare m-g-C_3N_4, the removal rate was 75%, 94%, 93%, and 3% for amoxicillin, cefotaxime, meropenem, and sulbactam, respectively. The PDS degradation system only for amoxicillin, cefotaxime, meropenem, and sulbactam measured 50%, 81%, 80%, and 6%, respectively, at neutral pH. The maximum photodegradation of antibiotics obtained in the PDS/m-g-C_3N_4 photocatalytic system was attributed to the presence of more $SO_4^{\bullet-}$ and $OH^{\bullet}$ reactive species. However, the minimal removal rate of sulbactam antibiotics was further investigated at different pH as presented in Fig. 5b, which indicated pH 4.0 to be most efficient in 71% removal of sulbactam. The improved photo removal efficiency under acidic solution is due to the unsymmetrical cleavage of protonated PDS; $HS_2O_8^{-2}$ by S-O bond breakage rather than O–O bond and led to the formation of bisulfide; HSO_3^- ions, which weakened the stable thiazole ring of sulbactam. This work signified the vital role of pH during PDS

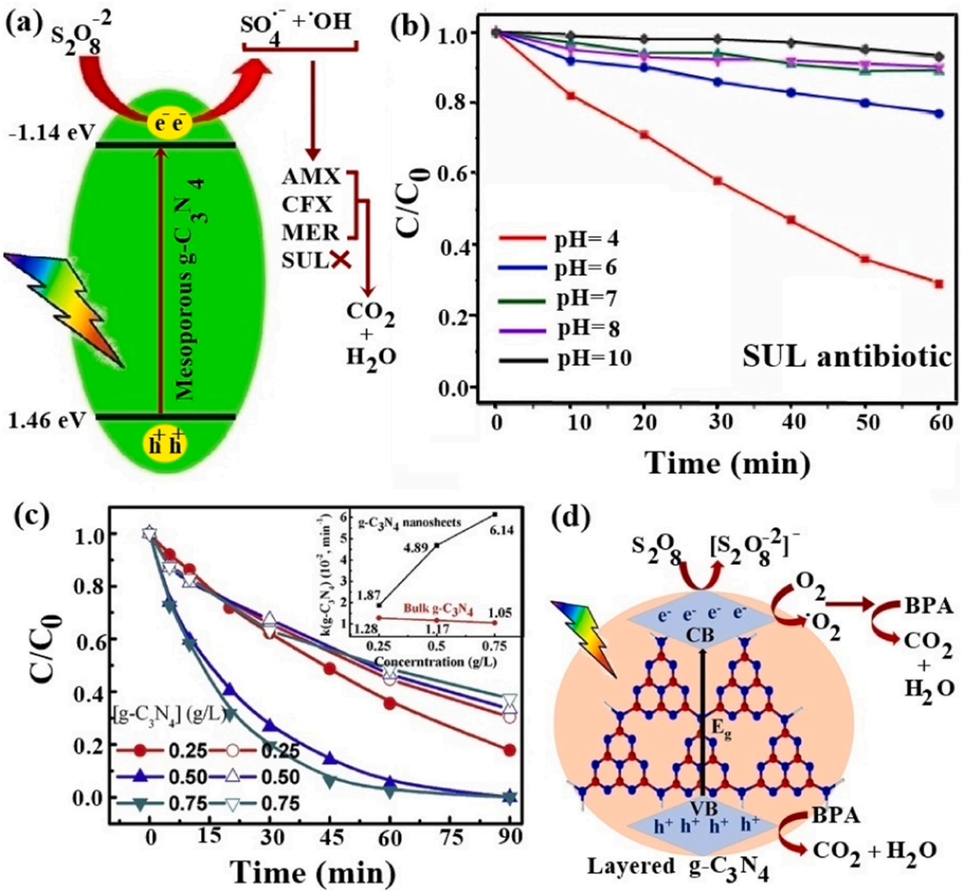

Fig. 5. (a) Plausible photodegradation mechanism of β-lactam antibiotics, i.e., amoxicillin (AMX), cefotaxime (CFX), meropenem (MER) over PMS/mesoporous g-C_3N_4 photocatalytic system, (b) effect of pH variation on photodegradation of sulbactam (SUL) antibiotic, (c) effect of bulk and nanosheets g-C_3N_4 dosages on bisphenol A degradation, represented by open and closed symbols, respectively (d) possible photodegradation mechanism of bisphenol A over PDS/ layered g-C_3N_4 photocatalyst.
Reprinted with permission from Refs. Dou et al. (2020) and Liu et al. (2017). License No. 4871780664899 and 4871780438032.

cleavage for sulbactam photodegradation in addition to the action of reactive oxidative species (Dou et al., 2020).

PDS electron acceptor nature was explored for the photodegradation of bisphenol A over bulk g-C_3N_4, and exfoliated layered g-C_3N_4 framework resulted in 22% and 72.5% bisphenol A photodegradation within 90 min of visible irradiation. However, PDS addition to both the systems improved the removal efficiency to 77% and 100% for bulk g-C_3N_4/PDS and layered g-C_3N_4/PDS, respectively. The g-C_3N_4 concentration also played a significant role, as illustrated in Fig. 5c, which showed 100% bisphenol A removal at 0.5 g/L dosages of nanosheets g-C_3N_4. In contrast, at 0.25 g/L concentration, a decreased degradation of 82.2% bisphenol A was attained. However, a maximum of 70% bisphenol A degradation was obtained on varying the bulk g-C_3N_4 concentration from 0.25 to 0.75 g/L. The obtained results are due to the PDS-captured photoinduced electrons of layered g-C_3N_4 and reduced electron-hole pairs recombination. The highly reductive electrons and PDS reduced molecular O_2 into $O_2^{\bullet -}$ which participated in the photodegradation of bisphenol A into CO_2 and H_2O, as illustrated in Fig. 5d and explained in the following Eqs. (1)–(6) (Liu et al., 2017).

$$g-C_3N_4+h\nu\rightarrow \quad e^-+h^+ \tag{1}$$

$$g-C_3N_{4e-} \quad +O_2\rightarrow O_2^- \tag{2}$$

$$g-C_3N_{4e-} \; +S_2O_8^{-2}\rightarrow\left[S_2O_8^{-2}\right]^- \tag{3}$$

$$\left[S_2O_8^{-2}\right]- \quad +O_2 \quad \rightarrow S_2O_8^{-2} \quad + \quad O_2^- \tag{4}$$

$$O_2^-+BPA \quad \rightarrow CO_2 \quad + \quad H_2O \tag{5}$$

$$g-C_3N_{4h+} \quad +BPA \quad \rightarrow CO_2 \quad + \quad H_2O \tag{6}$$

In a similar mechanistic route, Song et al. achieved 98.4% in photodegradation of sulfamethoxazole antibiotic using the PDS/g-C_3N_4 photocatalyst (60 min, stimulating sunlight) (Song et al., 2020).

It notes that the mechanism of PMS activation over g-C_3N_4 depends on the wavelength of solar light radiation. Typically, $O_2^{\bullet -}$ radical, released at 254 nm over PMS/g-C_3N_4 photocatalyst, could not react with dimethyl phthalate pollutant, as shown in Fig. 6a. Whereas visible irradiations (< 420 nm) caused 90% photodegradation of dimethyl phthalate, which is mainly attributed to attacking aromatic benzene ring through $SO_4^{\bullet -}$ radical and hydroxylation of aliphatic chains via $OH^\bullet$ radical (Xu et al., 2020). The concentration of PMS affects significantly impacts the operational experiment cost and photodegradation efficiency. As shown in Fig. 6b, the photodegradation results revealed 26% in removing acidic orange 7 dye in the absence of PMS. After PMS was added and concentration was varied from 0.05 to 0.8 g $L^{-1,}$ the acidic orange 7 elimination rate was improved significantly from 39% to 86%. This phenomenon is attributed to the release of abundant reactive species under a higher PMS oxidant concentration, as explained in Eqs. (7)–(13)

$$g-C_3N_4+h\nu\rightarrow \quad e^-+h^+ \tag{7}$$

$$O_2+ \quad e^-\rightarrow O_2^- \tag{8}$$

$$HSO_5^-+ \quad O_2^- \quad \rightarrow SO_4^- \quad +HO_2^- \tag{9}$$

$$HSO_5^- \quad + \quad e^- \quad \rightarrow \quad SO_4^-+OH^- \tag{10}$$

$$HSO_5^- \quad + \quad h^+\rightarrow \quad SO_5^-+H^+ \tag{11}$$

$$2SO_5^-\rightarrow 2SO_4^- \quad +O_2 \tag{12}$$

$$SO_4^-+AO7 \quad dye \quad \rightarrow Inorganicions+CO_2 \quad + \quad H_2O \tag{13}$$

From the above plausible degradation mechanism, it was inferred that has reasonably low valence band potential makes it incapable of generating $OH^\bullet$ directly. This phenomenon leads to the direct oxidation reaction of HSO_5^- with holes to produce $SO_5^{\bullet -}$ and simultaneously enhanced production of photoinduced electrons, $SO_4^{\bullet -}$ and $O_2^{\bullet -}$. Hence, the acidic orange 7 removal efficiency could reach 86% within 30 min under visible light irradiation (Tao et al., 2015). In another study, Jiang et al. reported the influence of solution pH variations on acidic orange 7 degradation with PMS/g-C_3N_4 photocatalyst, as revealed in Fig. 6c (Jiang et al., 2017). In the acidic condition (pH of 3.51), acidic orange 7 dye removal could reach nearly 95% within 30 min. However, increasing the pH would lead to a decrease in the degradation rate. On

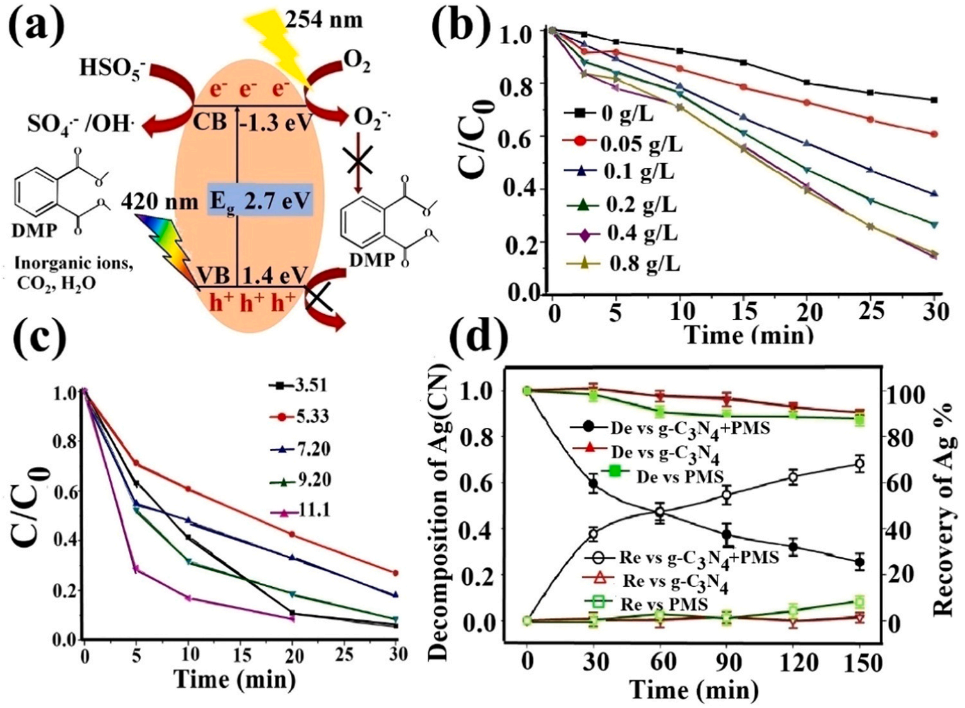

Fig. 6. (a) Plausible photodegradation mechanism of dimethyl phthalate (DMP) over PMS/ g-C_3N_4 photocatalyst, (b) influence of PMS concentration on acidic orange 7 degradation with PMS/ g-C_3N_4 photocatalyst, (c) effect of pH variation on acidic orange 7 degradation with PMS/g-C_3N_4 photocatalyst and (d) decomposition (De) of Ag $(CN)_2^{-1}$ and simultaneous recovery (Re) of Ag with bare g-C_3N_4, PMS systems, and PMS/g-C_3N_4 photocatalyst under 400 nm visible light.

Reprinted with permission from Refs. Xu et al. (2020), Tao et al. (2015), Jiang et al. (2017) and Qiao et al. (2020). License No. 4871790254437 and 4871790497800.

the other hand, acidic orange 7 degradation could nearly achieve 100% removal within 20 min in the strong alkaline condition. Jiang et al. (2017) proposed that the facile static interactions between host g-C_3N_4 and negatively charged PMS and acidic orange 7 in alkaline medium and the repulsive effect in the highly acidic medium are the two reasons to influence the degradation efficiency of target contaminant. In another approach, Qiao et al. reported the decomposition of silver cyanide complex $Ag(CN)_2^-$ and simultaneous recovery of Ag, obtained by photocatalytic activation of PMS over pristine g-C_3N_4 nanosheets (Qiao et al., 2020). As illustrated in Fig. 6d, only 10% decomposition of Ag $(CN)_2^-$ was obtained within 150 min, under visible light irradiation (400 nm) over the bulk g-C_3N_4 and PMS systems separately, corresponding to less than 10% Ag recovery rate. Whereas, in the PMS/g-C_3N_4 photocatalytic system, 74% of Ag $(CN)_2^-$ could be decomposed, corresponding to 68% Ag recovery, in the same conditions. Qiao et al. proposed that the release of $SO_4^{\bullet-}$ and $OH^{\bullet}$ reactive species plays a critical factor in this case (Qiao et al., 2020). Table S2 describes PMS/PDS activation using unmodified g-C_3N_4 photocatalyst (Dou et al., 2020; Liu et al., 2017; Song et al., 2020; Xu et al., 2020; Tao et al., 2015; Jiang et al., 2017; Qiao et al., 2020).

3. Heterojunction g-C_3N_4 for enhanced photocatalytic activation of PDS and PMS

Heterojunction formation has been developed as an effective strategy for maximum UV and visible light absorption and minimizing electron-hole pairs recombination. Semiconductor heterojunction construction proceeds through the stacking up of two semiconductors exhibiting different bandgap (Sonu et al., 2019). Different heterojunction systems pursue different charge transfer photocatalysis mechanisms based on the different electronic band positions of semiconductors. The most significant charge separation is followed by type-II heterostructure (Raizada

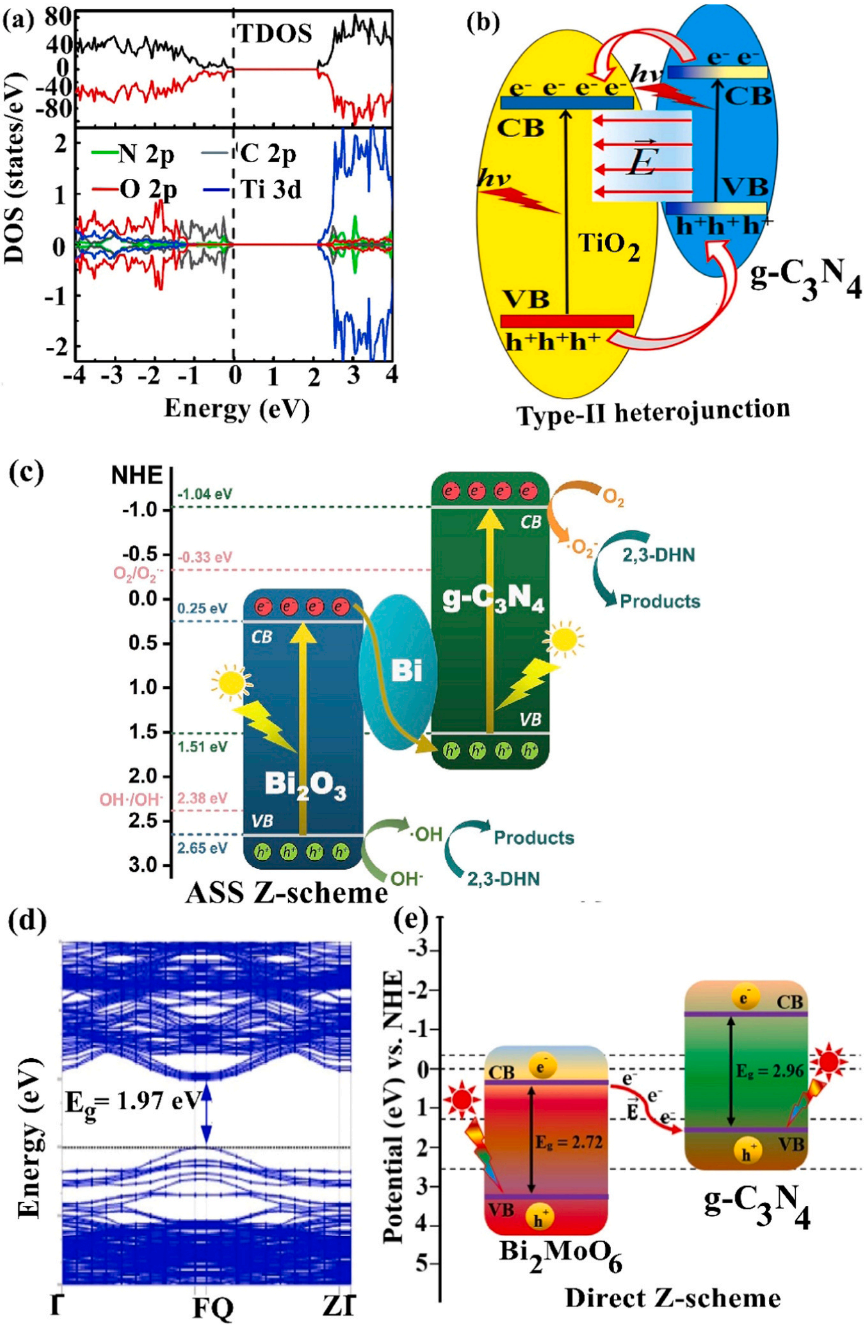

Fig. 7. (a) Total and partial density of states of g-C_3N_4/TiO_2 heterojunction, (b) charge stimulation mechanism of photocatalytic water splitting in g-C_3N_4/TiO_2 heterojunction, (c) illustration of 2,3-dihydroxynaphthalene (2,3-DHN) photodegradation by Bi mediated all-solid-state Z-scheme Bi@β-Bi_2O_3/g-C_3N_4 under visible light, (d) calculated band construction of g-C_3N_4/$BiMoO_6$ based on hybrid HSE06 functional theory, and (e) photocatalytic charge transference mechanism of g-C_3N_4/$BiMoO_6$ heterojunction. Reprinted with permission from Refs. Lin et al. (2017), Chen et al. (2019) and Opoku et al. (2018). License No. 4882360669924, 4882920616596, and 4882360829504.

et al., 2019b), where the conduction band and valence band of one semiconductor are higher than that of the other. There is an opposite migration of electrons and holes. Amongst these traditional heterojunctions, type-II heterostructure construction has been commonly approached charge transfer routes due to its spatial migration and maximum electron-hole pairs separation. Lin et al. proved facile charge carrier transference in $g\text{-}C_3N_4/TiO_2$ type-II heterostructure using spin-polarized DFT+U calculations. The conduction band minima of $g\text{-}C_3N_4/TiO_2$ heterostructure was occupied by Ti 3d orbitals whereas, C 2p, N 2p orbitals of $g\text{-}C_3N_4$ dominated valence band maximum instead of O 2p, as illustrated in Fig. 7a. On solar light illumination, the valence band electrons of $g\text{-}C_3N_4$ were transferred to the conduction band of TiO_2 with simultaneous migration of photogenerated holes from the valence band of TiO_2 to the valence band of $g\text{-}C_3N_4$, thus restraining the energy-wasting electron-hole pairs recombination process as shown in Fig. 7b (Lin et al., 2017).

A semiconductor with a lower bandgap is considered an ideal parameter for photocatalysis. Subsequently, a novel Z-scheme photocatalytic system results in more negative conduction band potential and more positive valence band potential full solar light response in the entire solar spectrum (Jin et al., 2020a). Z-scheme-driven photocatalysis is categorized into three main generations, which are explained as follows: Firstly, the redox mediator is driven (IO_3^-/I^-, Fe^{3+}/Fe^{2+}, NO_3^-/NO_2^-, etc.). For the generation-I, the Z-scheme mechanism proceeds via a combination of photo-illuminated electrons in the conduction band of semiconductor-II (SC-II) with holes in the valence band of semiconductor-I (SC-I) (Jourshabani et al., 2020; Bai et al., 2020). This phenomenon leads to the formation of strongly oxidative valence band holes in SC-II and reductive conduction band electrons in SC-I, and enhanced electron-hole pairs separation. Secondly, the generation-II Z-scheme is an all-solid-state photocatalytic system. They are designed by combining two semiconductors and an electron mediator, usually noble metal, i.e., Ag, Au, Pt, etc., at the interface to lower charge recombination probability (Cao et al., 2017). Unusually employed, bismuth (Bi) served as an electron bridge facilitating the temporal separation of photogenerated charge carriers in $\beta\text{-}Bi_2O_3/$ $g\text{-}C_3N_4$ all-solid-state Z-scheme heterojunction. As presented in Fig. 7c, the photoexcited electrons in the conduction band of $\beta\text{-}Bi_2O_3$ transferred to the valence band of $g\text{-}C_3N_4$ via Bi-metal bridge and maintained the inherent oxidation and reduction abilities correlative components (Lan et al., 2020). However, the electron shuttle mediator tends to absorb photons, limiting the photocatalytic heterojunction system. Hence, in the generation-II, I direct Z-scheme photocatalyst, the two semiconductors form a direct surface junction with each other omitting the requirement of redox mediators or noble metals interface (Chen et al., 2019). The interfacial charge combination is realized due to weak Van der Waals interaction and internal electric field existence between two semiconductors (Adhikari et al., 2020). The direct Z-scheme heterostructures are designed to function as a sieve for consumed photoexcited electron-hole pairs with low redox potential, reducing the light-shielding effect and improving redox ability. The DFT computations for band structure determination of $g\text{-}C_3N_4/Bi_2MoO_6$ illustrated in Fig. 7d were evident in the direct Z-scheme charge transfer route. The indirect bandgap of bulk Bi_2MoO_6 was 2.72 eV; similarly, bulk $g\text{-}C_3N_4$ has an indirect bandgap (2.73 eV) with conduction band minima located at Γ point and valence band maximum at K point. Upon forming $g\text{-}C_3N_4$ $/Bi_2MoO_6$ Z-scheme heterostructure, there was a transition of indirect-gap to direct-gap due to introduced strains in the valence band $g\text{-}C_3N_4$. This direct bandgap was beneficial for transferring electrons from the conduction band of Bi_2MoO_6 to the valence band of $g\text{-}C_3N_4$, as shown in Fig. 7e (Opoku et al., 2018). Recently, various well-designed $g\text{-}C_3N_4$ based heterostructures have been synthesized for photodegradation applications via PMS/PDS photocatalytic activation.

3.1. *Type-II heterostructures*

The staggered band alignment between $g\text{-}C_3N_4$ and other semiconductors facilitates electron-hole pairs transportation and induces an electric field in the heterojunction region (Ren et al., 2019). This is due to the highest negative conduction band position of $g\text{-}C_3N_4$, i.e., − 1.17 V, making it a stronger reductive photocatalyst than other photocatalysts. To date, $g\text{-}C_3N_4$ based type-II heterostructures have provided synergistic results for PMS/PDS photocatalytic activation targeted for pollutant photodegradation. For instance, as demonstrated in Fig. 8a, the coupled $g\text{-}C_3N_4/CeO_2$ photocatalyst combined with PDS followed the facile migration of electrons from − 1.17 V conduction band of $g\text{-}C_3N_4$ to − 0.35 V conduction band of CeO_2, while the holes of CeO_2 transferred to the valence band of $g\text{-}C_3N_4$. This charge transfer route allowed maximum separation of electron-hole pairs and significant release of $O_2^{\bullet-}$, $SO_4^{\bullet-}$ and OH radicals, which contributed to the rapid degradation of norfloxacin antibiotics. This is evidenced by the photocatalytic efficiency results shown in Fig. 8b, where PDS alone could not degrade norfloxacin in 60 min of irradiations. Similarly, only 24.3% and 13.8% norfloxacin were degraded by bare $g\text{-}C_3N_4$ and CeO_2 due to their large bandgap of 2.7 and 2.8 eV, respectively. After coupling both semiconductors, 46.1% norfloxacin degradation was obtained in 5% $g\text{-}C_3N_4/CeO_2$ photocatalytic system. Improvement in photocatalytic norfloxacin removal efficiency up to 60.9% and 52.7% was observed on PDS oxidant addition. An optimum concentration of 5 mM PDS in 5% $g\text{-}C_3N_4/CeO_2$ enhanced degradation efficiency to 88.6% within 60 min of irradiations, attributed to the release of $SO_4^{\bullet-}$ oxidizing species on the reaction of PDS with photogenerated electrons (Liu et al., 2020b). The quasi-full-visible light absorption power of dye-sensitized D35 was complemented with $g\text{-}C_3N_4/TiO_2$ heterojunction for synergistic PDS photocatalytic activation. The synthesized $g\text{-}C_3N_4/TiO_2$/D-35/PDS photocatalyst eliminated acetaminophen, methylene blue dye, and caffeine within 30 min of 675 nm irradiations via the following photocatalytic electron transfer processes as shown in Eqs. (14)–(19)

$$g - C_3N_4 + h\nu \rightarrow g - C_3N_{4e-} + g - C_3N_{4h+} \tag{14}$$

The holes in the valence band of $g\text{-}C_3N_4$ with potential 1.79 V directly participate in bisphenol A degradation, whereas electrons of $g\text{-}C_3N_4$ are transferred to the conduction band of TiO_2 (−0.75 V).

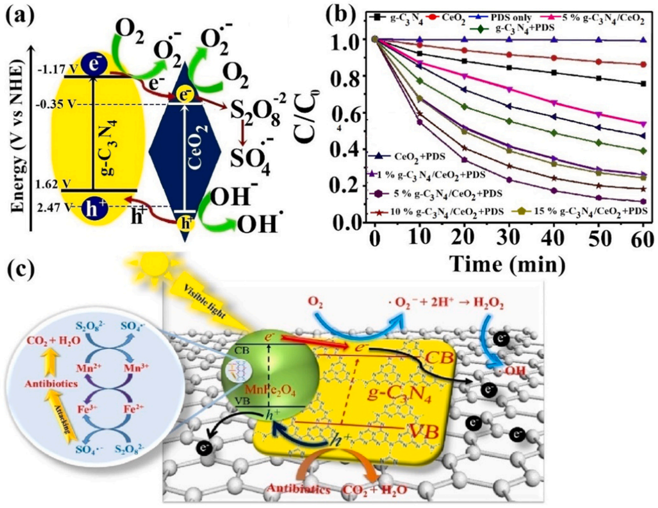

Fig. 8. (a) Photoactivation of PDS; $S_2O_8^{-2}$ over $g\text{-}C_3N_4/CeO_2$ type-II heterostructure, (b) norfloxacin degradation curves by the photocatalysts with and without PDS oxidant, and (c) mechanism for antibiotics degradation over $MnFe_2O_4$/ $g\text{-}C_3N_4$/PDS/vis photocatalytic system.

Reprinted with permission from Refs. Liu et al. (2020a) and Wang et al. (2017a). License No. 4872600011574 and 4872600360582.

$$TiO_{2\ e-} + S_2O_8^{2-} \rightarrow SO_4^{\bullet -} + SO_4^{2-} \tag{15}$$

$$SO_4^{\bullet -} + H_2O \rightleftarrows OH^{\bullet} + HSO_4^{-} \tag{16}$$

$$TiO_{2e-} + O_2 \rightarrow O_2^{\bullet -} \tag{17}$$

$$TiO_{2e-} + O_2^{-} + 2H^{+} \rightarrow OH^{\bullet} + OH^{-} \tag{18}$$

$$D35 + h\nu \rightarrow D35_{e-} + D35_{h+} \tag{19}$$

The $D35_{e-}$ with a potential of − 1.37 V are transferred to the conduction band of TiO_2 while holes of D35 participate in the direct oxidation of bisphenol A. The process confirmed the extensive participation of four reactive species, i.e., $SO_4^{\bullet -}$, $OH^{\bullet}$, $O_2^{\bullet -}$ and holes (Yang et al., 2019). Similarly, these reactive species' role was observed in p-n heterojunction between $MnFe_2O_4$ and g-C_3N_4/PDS supported on graphene targeted for photodegradation of antibiotics. The oxidation of Mn^{2+}, Fe^{2+} results in effective activation of PDS, and the facile charge migration, as illustrated in Fig. 8c, resulted in 91.5% elimination of metronidazole, amoxicillin, tetracycline, ciprofloxacin within 60 min of 450 nm irradiations (Wang et al., 2017a).

The dual functionality of g-C_3N_4 to serve as an electron acceptor and PMS activator was observed in multi-layered CoAl-LDH/g-C_3N_4 type-II heterostructure, as demonstrated in Fig. 9a. The transference of electrons from the conduction band of CoAl-LDH (−1.14 eV) to the conduction band of g-C_3N_4 (−1.06 eV) promoted the release of $O_2^{\bullet -}$, with the simultaneous reaction of photogenerated electrons with PMS. Also, Co^{2+} participated in the generation of $SO_4^{\bullet -}$ as explained in the following Eqs. (20) and (21)

$$Co^{3+} + HSO_5^{-} \rightarrow Co^{2+} + SO_5^{\bullet -} + H^{+} \tag{20}$$

$$Co^{2+} + SO_4^{\bullet -} \rightarrow Co^{3+} + SO_4^{-} \tag{21}$$

The effectively produced $SO_4^{\bullet -}$, $OH^{\bullet}$, and $O_2^{\bullet -}$ contributed to 87.1% photodegradation of sulfadiazine within 15 min of 450 nm irradiations (Zeng et al., 2020). The coupled activated carbon/g-C_3N_4 heterostructure possessed a higher specific surface area of 192 $m^2\ g^{-1}$ and a lowered band gap of 2.65 eV compared to 73 $m^2 \cdot g^{-1}$ and 2.75 eV of bare g-C_3N_4. The as-synthesized 5 mM PMS/activated carbon / g-C_3N_4 led to 98.7% atrazine removal whereas bare g-C_3N_4 obtained only 3.91%, 7.3%, 57.9% and 78.76%, 5% activated carbon/ g-C_3N_4, 30% activated carbon/ g-C_3N_4 and g-C_3N_4/PMS photocatalytic system within 120 min of 465 nm visible irradiations. The higher photocatalytic efficiency was due to the electron acceptor, the transporter nature of activated carbon, and the subsequent acceptance of PMS electrons to generate highly reactive $SO_4^{\bullet -}$ and $OH^{\bullet}$ radical (Dikdim et al., 2019). g-C_3N_4 modified Fe_2O_3 was employed for the photocatalytic activation of PMS to improve the photodegradation of acidic orange 7 dye. An increased surface area of 97 $m^2\ g^{-1}$ was obtained for g-C_3N_4/Fe_2O_3 photocatalyst compared to 30 $m^2\ g^{-1}$ of bare g-C_3N_4, as presented in Fig. 9b N_2 adsorption-desorption isotherm curve. The increased surface area provided more reactive sites for 98.5% acidic orange 7 elimination within 20 min of 420 nm visible irradiations, whereas the bare PMS could not degrade acidic orange 7 dye (Li et al., 2017). Similarly, g-C_3N_4/Mn_3O_4 heterojunction was targeted for phenol removal via PMS photocatalytic activation. As shown in Fig. 9c, the photocatalytic efficiency results revealed negligible phenol degradation in PMS only, g-C_3N_4/PMS, and g-C_3N_4/Mn_3O_4 composites suggestive of inactivated PMS. However, g-C_3N_4/Mn_3O_4/PMS composite degraded 87.3% phenol within 60 min of 420 nm irradiations due to photogenerated electrons in redox reactions of Mn^{2+}/Mn^{3+} and Mn^{3+}/Mn^{4+}, which led to PMS photocatalytic activation and production of $SO_4^{\bullet -}$ and $OH^{\bullet}$ reactive species

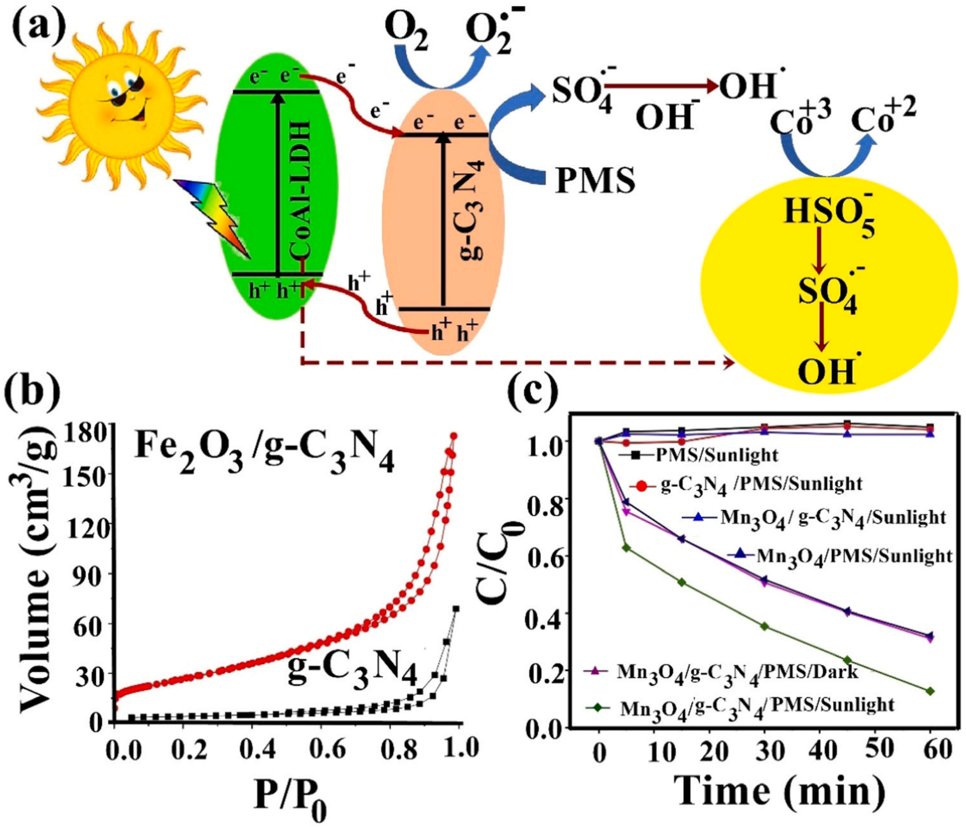

Fig. 9. (a) Schematic diagram of a mechanism for sulfadiazine (SDZ) degradation by PMS assisted CoAlLDH/ g-C_3N_4 type-II photocatalytic system. (b) N_2 adsorption-desorption isotherms of g-C_3N_4 and Fe_2O_3/g-C_3N_4. (c) The degradation efficiency of phenol over different photocatalytic systems.
Reprinted with permission from Refs. Zeng et al. (2020), Li et al. (2017) and Chai et al. (2019). License No. 4872601283863 and 4872610331932.

(Chai et al., 2019).

However, type-II heterojunction provided minimum reduction and oxidation abilities to charge carriers. The major drawback of rapid electron-hole pairs recombination was persistent in some combination of semiconductors with g-C_3N_4 (Du et al., 2020). Moreover, the migration of electrons and holes towards a similar space charge region could be hindered by electrostatic repulsion between hole-hole and electron-electron charges (Guo et al., 2018; Gong et al., 2018). Therefore, the asserted charge transfers in type-II is doubtful. In contrast, the Z-scheme heterojunction photocatalytic systems feature a configuration in which electrons in the lower conduction band of one semiconductor can be combined with holes on another semiconductor.

3.2. All-solid-state driven g-C_3N_4 based photocatalysts

The all-solid-state Z-scheme heterojunctions are functional in both liquid and gas phases accompanied by facile charge transfer via noble metal, which serves as a bridge at the interface area between two semiconductors. The two approaches for the all-solid-state Z-scheme construction are an in-situ formation of electron mediators using silver halides (AgX), where X represents halides, i.e., Br, Cl, and I. The instability of AgX has led to the direct anchoring of Ag nanoparticles on semiconductors by precipitation and photodeposition methods (Xue et al., 2020). Jin and co-workers photodeposited Ag nanoparticles on MoS_2 nanosheets coupled with g-C_3N_4 for enhanced PMS mediated photocatalytic tetracycline degradation, as presented in Fig. 10a. The Z-scheme charge transfer mechanism over MoS_2/Ag/g-C_3N_4 photocatalyst involved transference of electrons from the conduction band of MoS_2 (−0.30 eV) to Ag metal. Simultaneously, to maintain the Ag Fermi level equilibrium, there was a migration of holes from the valence band of g-C_3N_4 (+1.69 eV) to Ag metal, where electron-hole pairs recombination occurred. The highly reductive electrons in the conduction band of g-C_3N_4 (−1.04 eV) released $O_2^{\bullet-}$ and PMS trapped the remaining photoinduced electrons for subsequent $SO_4^{\bullet-}$ and $OH^{\bullet}$ radicals formation confirmed by electron paramagnetic resonance analysis Fig. 10b with DMPO as spin trapping agent. The ensured effective charge separation was interpreted by a smaller semi-circular arc radius for MoS_2/Ag/g-C_3N_4, as shown in Fig. 10c electrochemical impedance spectra. The synergistic action of reduced electron-hole pairs recombination and attack of $O_2^{\bullet-}$, $SO_4^{\bullet-}$ and $OH^{\bullet}$ species led to 98.9% tetracycline photocatalytic degradation within 50 min 420 nm visible irradiations (Jin et al., 2020b).

The essence of the highest photocatalytic levofloxacin degradation is assisted by PMS oxidant in Ag/AgCl@ZIF-8/g-C_3N_4 (AZ-g-C_3N_4) composite. This is evidenced by the degradation trend in the following photocatalysts, ZIF-8 (4.7%) > Ag/AgCl@ZIF-8 (15.3%) > g-C_3N_4 (20%) > Ag/AgCl@ZIF-8/PMS (38.9%) > 10% AZ-g-C_3N_4 (53.6%), g-C_3N_4/PMS (66.2%). A maximum of 87.3% levofloxacin degradation was obtained over 10% AZ-g-C_3N_4 with 2 mM PMS after 60 min of 450 nm irradiations. The factors contributing to enhanced levofloxacin photodegradation are the increased surface area (porous ZIF-8 metal-organic framework composite) and the maximized electrons transfer efficiency (the lowest peak for 10% AZ-g-C_3N_4 in photoluminescence spectra, displayed in Fig. 10d). Additionally, the Ag nanoparticles mediated facile charge transfer route between the conduction band of g-C_3N_4, AgCl, and ZIF-8 effectively released $O_2^{\bullet-}$, $SO_4^{\bullet-}$ and $OH^{\bullet}$ for levofloxacin degradation (Zhou et al., 2019). Due to the high cost of noble metal electron mediators and photo corrosive nature, they are being replaced by non-noble metals such as Cu (Zuo et al., 2017) and carbonaceous materials (CNTs and C_{60}, etc.) (Ma et al., 2017). Although the storage of photoinduced electrons in electron mediators improves the separation of the electron-hole pairs but reduces the number of electrons for the PMS photocatalytic activation. Also, it is not easy to guarantee the position of electrons mediators between the two photocatalysts.

3.3. Direct Z-scheme

A direct Z-scheme mechanism was developed to suppress the backward reactions and shielding effect of charge carrier mediators in generation I and II Z-scheme photocatalytic systems. The close contact

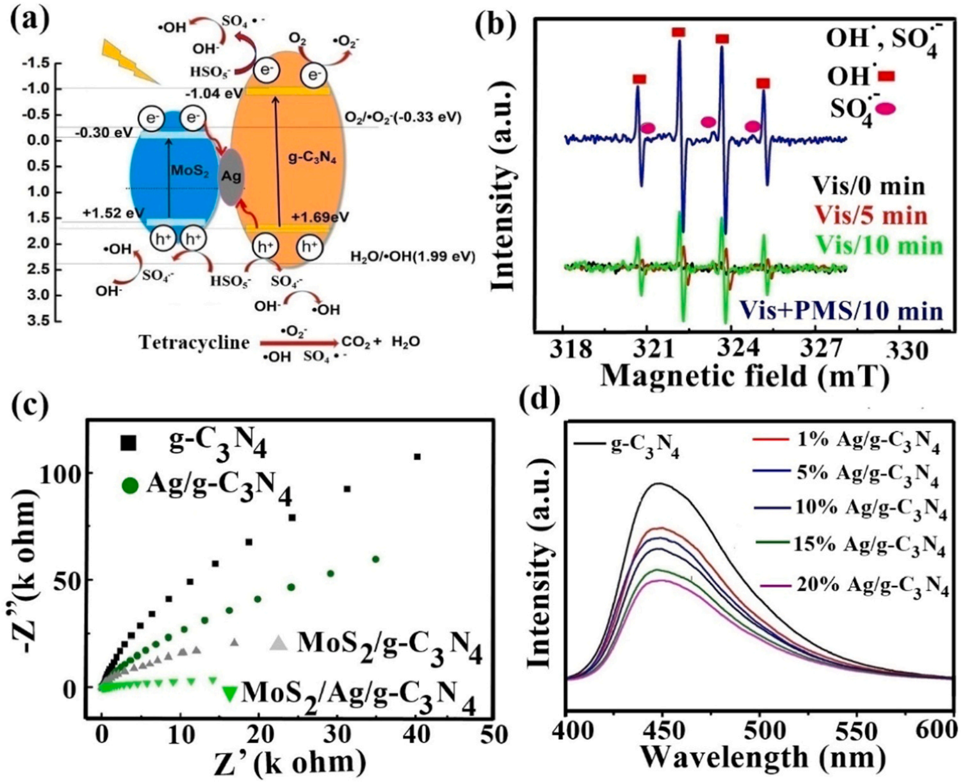

Fig. 10. (a) Proposed mechanism for tetracycline degradation by PMS assisted MoS_2/Ag/g-C_3N_4/Vis all-solid-state Z-scheme photocatalytic system, (b) Electron spin resonance spectra of MoS_2/Ag/g-C_3N_4/PMS system in the presence of DMPO, (c) Electrochemical impedance spectroscopy (EIS) of different photocatalysts, and (d) Photoluminescence spectra of Ag/AgCl@ZIF-8/g-C_3N_4 (AZ-g-C_3N_4) composite.
Reprinted with permission from Refs. Jin et al. (2020a) and Zhou et al. (2019). License No. 4872620612758 and 4872620902639.

between semiconductors without charge carrier transfer mediators induces an electric field with more vital redox ability for electron-hole pairs redistribution. Also, Z-scheme photocatalysts possess spatially separated reductive and oxidative sites for improved electron-hole pairs separation (Stelo et al., 2020). For instance, g-C_3N_4 coupled with perylene imide (PI) prepared via an amidation reaction of perylene tetracarboxylic dianhydride (PTCDA) followed a direct Z-scheme charge migration pathway, as illustrated in Fig. 11a. The facile transference of electrons from the conduction band of PTCDA into the valence band of g-C_3N_4 reduced electron-hole pairs recombination. The photoinduced holes in the valence band of PTCDA directly oxidized bisphenol A while the PMS photocatalytic activation occurred via electrons in g-C_3N_4 for the significant release of $SO_4^{\bullet-}$ and $OH^\bullet$ reactive species. The bisphenol A photodegradation was analyzed over different photocatalysts with corresponding results were 5%, 6%, 29% for PTCDA, pristine g-C_3N_4, and g-C_3N_4/PI, respectively. Whereas 96% bisphenol A elimination was obtained on the addition of 5 mM PMS in 5% g-C_3N_4/PI photocatalyst within 60 min of 400 nm irradiations (Zhang et al., 2018). The presence of photoactivated PMS diclofenac antibiotic was completely eliminated over g-C_3N_4/Co_3O_4 within 30 min of visible light irradiations. This result was attributed to the release of $SO_4^{\bullet-}$ and $OH^\bullet$ radicals in the presence of 0.05 M EtOH and tert-butyl alcohol (TBA) with 60% and 80% removal efficiency, respectively, as confirmed by the radical scavenging experiment results displayed in Fig. 11b. Also, Z-scheme mechanistic illustration in Fig. 11c and Eqs. (22)–(25) evinced PMS photocatalytic activation via both the electrons of g-C_3N_4 and holes of Co_3O_4 with effective charge separation (Shao et al., 2017).

$$g-C_3N_4/Co_3O_4 \quad +h\vartheta\rightarrow \quad CBe^- \quad +VBh^+ \tag{22}$$

$$HSO_5^- \quad +g-C_3N_{4\,CBe-}\rightarrow SO_4^{\bullet-}+OH^- \tag{23}$$

$$HSO_5^- +g-C_3N_{4\,VBh+} \quad \rightarrow \quad SO_5^{\bullet-}+H^+ \tag{24}$$

$$SO_4^{\bullet-}+ \quad OH^\bullet +DCF\rightarrow \quad CO_2+H_2O \tag{25}$$

The capability of photoactivated PMS was exploited for carbamazepine antibiotic photodegradation via g-C_3N_4 coordinated iron hexadecachlorophthalocyanine ($FePcCl_{16}$) supported on isonicotinic acid (INA). The photocatalytic efficiency results revealed 94%, 55%, 49% and 3.6% carbamazepine removal rate over g-C_3N_4-INA-$FePcCl_{16}$/PMS, g-C_3N_4/PMS, g-C_3N_4-$FePcCl_{16}$ and g-C_3N_4-INA-$FePcCl_{16}$ photocatalyst within 40 min of 420 nm irradiations. The effect of diverse pH was investigated, as shown in Fig. 11d. The acidic pH of 5 significantly enhanced the carbamazepine degradation up to 94%, while 80% was obtained at pH 7% and 65% at pH of 11, indicative of broader pH response-ability of g-C_3N_4-INA- $FePcCl_{16}$/PMS photocatalytic system over bare g-C_3N_4. Based on these results, PMS photocatalytic activation was considered the primary reason for 94% carbamazepine degradation. Also, the synergistic Z-scheme spatial charge separation mechanism involved the transference of conduction band electrons from $FePcCl_{16}$ to the conduction band of g-C_3N_4. This photogenerated electron was captured by PMS for the generation of reactive $SO_4^{\bullet-}$ which underwent reaction with OH^- and gained $OH^\bullet$ radical (Wu et al., 2017). This concludes our discussion to a perspective that selecting suitable semiconductors with appropriate band energy is a prerequisite for the successful formation of direct Z-scheme photocatalyst intended to preserve photogenerated electron-hole pairs with stronger redox abilities for PMS photocatalytic activation (Dong et al., 2019). g-C_3N_4 based heterostructures can effectively improve PMS/PDS photocatalytic activation to achieve high organic contaminant removal, as summarized in Table S3.

4. Summary and perspectives

In this review, we have intensively highlighted the superiority of $SO_4^{\bullet-}$ radical over other reactive oxidative species ($OH^\bullet$, $O_2^{\bullet-}$, and $^1O_2$ etc.) for the pollutant degradation by the photocatalytic activation of peroxydisulfate (PDS) and peroxymonosulfate (PMS) via metal-free g-C_3N_4-based photocatalysts. Following the current research progress, the photocatalysis is shifting towards the use of $SO_4^{\bullet-}$ due to the unique properties of high oxidation potential (2.5–3.1 V), stability, selectivity, and applicability in a wide pH range. Without any doubt, both PDS and PMS are a promising source of $SO_4^{\bullet-}$ and $OH^\bullet$ radicals. The mechanistic details of metal-free g-C_3N_4 based PMS/PDS photocatalytic activation

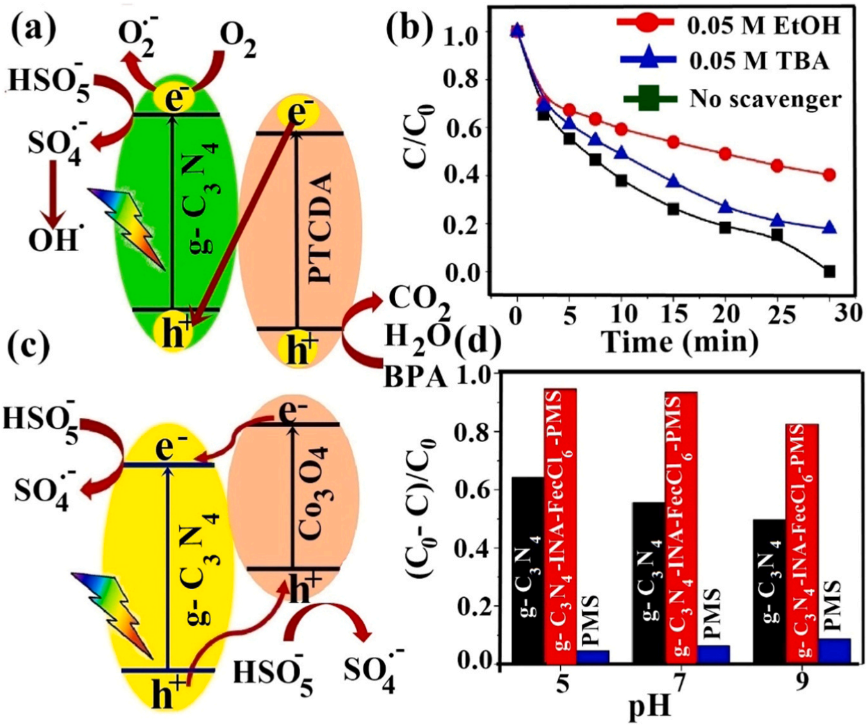

Fig. 11. (a) The plausible photocatalytic mechanism in the PI/g-C_3N_4/PMS/Vis Z-scheme system. (b) The effect of radical scavengers on diclofenac degradation over g-C_3N_4/Co_3O_4/PMS photocatalyst. (c) The possible photoactivation mechanism of the g-C_3N_4/Co_3O_4 composite with PMS under visible light irradiation. (d) The removal rate for photocatalytic degradation of carbamazepine over g-C_3N_4-INA-$FePcCl_{16}$/PMS photocatalyst.
Reprinted with permission from Refs. Zhang et al. (2018), Shao et al. (2017) and Wu et al. (2017). License No. 4872631190726 and 4872631462917.

under light irradiations have been successfully illustrated. The insightful understanding of heterojunction formation in g-C_3N_4 for extended visible light absorption and minimized charge carrier recombination and extended radical action are typically elaborated. Notably, the type-II heterostructures represent a synergistic relationship between PMS/PDS and g-C_3N_4 photocatalysts. The further discussion provides influences of operational parameters, i.e., pH, the concentration of oxidants, and specific surface area for a significant release of $SO_4^{\bullet-}$ and $OH^{\bullet}$ via PMS/PDS photocatalytic activation. Finally, to overcome the current challenges, critical suggestions in both PMS/PDS photocatalytic activation mechanism exploration and g-C_3N_4 modifications are proposed.

Based on the analysis mentioned above, the photocatalytic PMS/PDS activation process is dominantly governed by the electron transfer between g-C_3N_4 (electron donors) and PMS/PDS (electron acceptors**)**. Noteworthily, the combined utilization of solar light, metal-free g-C_3N_4, and PMS/PDS as a source of $SO_4^{\bullet-}$ and $OH^{\bullet}$ is expected to be the promising way to drive the pioneering water purification technologies in the future. Despite PDS and PMS are powerful oxidants for the generation of $SO_4^{\bullet-}$, we find that PMS/PDS photocatalytic activation process via metal-free g-C_3N_4 suffers from some practical limitations:

- The specificity of predominant free radicals: Solar irradiation driven g-C_3N_4 based PMS/PDS photocatalytic activation involves the release of $SO_4^{\bullet-}$ as major reactive species. However, many studies claim the simultaneous release of $OH^{\bullet}$ and $O_2^{\bullet-}$ radicals. Sometimes conversion of $SO_4^{\bullet-}$ into other reactive species lowers the oxidative potential of $SO_4^{\bullet-}$. It is thus necessary to reveal the specific role of every reactive species for pollutant removal.
- The complexity of mechanism: Due to the multiple factors governing PMS/PDS photocatalytic activation process, g-C_3N_4 actual mechanism is still ambiguous. The co-existence of a radical and non-radical pathway in the same photocatalytic system needs conclusive pathway selectivity. The previously reported work has only focused upon the degradation of target pollutants by the released $SO_4^{\bullet-}$ and $OH^{\bullet}$ without assessing toxic by-products. Therefore, further studies should analyze the harmful effects of generated intermediates during PMS/PDS-mediated photodegradation processes.
- Toxicity of $SO_4^{\bullet-}$ radical: The excessive concentration of PMS/PDS is applied to obtain high pollutant degradation and inevitable $SO_4^{\bullet-}$ production in the water body beyond toxicity levels. More efforts should pay to address this issue to avoid any loss of oxidants by optimizing the stoichiometric reaction efficacy (RSE %).
- Conflicting charge transfer routes in heterojunctions: The tailoring g-C_3N_4 -based heterostructures is to acquire improved solar light absorption efficiency, leading to balance enhancing the photooxidative potential g-C_3N_4 and maintaining the high redox potentials of two photocatalysts. The type-II and Z-scheme heterojunctions are the two cutting-edge research hotspots. However, in-depth studies reveal debatable type-II charge transfer routes due to electrostatic repulsions between like charges. As for the all-solid-state Z-scheme photocatalytic systems, the position of the electron mediator is not particular. Undoubtedly in the direct Z-scheme, the charge migration pathway is entirely different. It tends to solve the predicaments of simultaneously possessing minimal charge carrier recombination rate and higher redox abilities; it lacks valid experimental evidence.

Based on this review's critical advances, highly efficient persulfate-activated g-C3N4 heterojunction-based photocatalysts will be beneficial in environmental remediation and other photocatalytic fields. Undoubtedly, substantial breakthroughs of persulfate-activated g-C_3N_4 heterojunction based photocatalysts toward environmental remediation are expected in the coming years.

CRediT authorship contribution statement

Vasudha Hasija: Conceptualization, Methodology, Investigation, Writing - original draft. **Van-Huy Nguyen**: Conceptualization, Methodology, Writing - review & editing. **Ajay Kumar**: Conceptualization, Methodology. **Pankaj Raizada**: Supervision, Conceptualization, Methodology, Investigation, Writing - original draft. **Venkata Krishnan**: Conceptualization, Methodology. **Aftab Aslam Parwaz Khan**: Conceptualization, Methodology. **Pardeep Singh**: Supervision, Conceptualization, Methodology, Investigation, Writing - original draft. **Eric Lichtfouse**: Conceptualization, Methodology, Writing - review & editing. **Chuanyi Wang**: Conceptualization, Methodology. **Pham Thi Huong**: Conceptualization, Methodology.

Declaration of Competing Interest

The authors declare that they have no known competing financial interests or personal relationships that could have appeared to influence the work reported in this paper.

Acknowledgments

Ajay Kumar is thankful to the Ministry of Education for the senior research fellowship. Venkata Krishnan acknowledges the Indian Institute of Technology Mandi for the research facilities.

References

Adhikari, S., Lee, H.H., Kim, D.H., 2020. Efficient visible-light induced electron-transfer in z-scheme $MoO_3/Ag/C_3N_4$ for excellent photocatalytic removal of antibiotics of both ofloxacin and tetracycline. Chem. Eng. J. 391, 123504.

Agustina, T.E., Ang, H.M., Vareek, V.K., 2005. A review of synergistic effect of photocatalysis and ozonation on wastewater treatment. J. Photochem. Photobiol. 6 (4), 264–273.

Bai, Y., Ye, L., Wang, L., Shi, X., Wang, P., Bai, W., Wong, P.K., 2020. g-$C_3N_4/Bi_4O_5I_2$ heterojunction with I_3^-/I^- redox mediator for enhanced photocatalytic CO_2 conversion. Appl. Catal. B Environ. 194, 98–104.

Bard, A.J., Parsons, R., Jordan, J., 1985. Standard Potentials in Aqueous Solution, , first ed.834. M. Dekker, New York.

Brillas, E., 2020. A review on the photoelectro-Fenton process as efficient electrochemical advanced oxidation for wastewater remediation. Treatment with UV light, sunlight, and coupling with conventional and other photo-assisted advanced technologies. Chemosphere 250, 126198.

Brillas, E., Segura, S.G., 2020. Benchmarking recent advances and innovative technology approaches of Fenton, photo-Fenton, electro-Fenton, and related processes: a review on the relevance of phenol as model molecule. Sep. Purif. Technol. 237, 116337.

Cao, S., Low, J., Yu, J., Jaroniec, M., 2015. Polymeric photocatalysts based on graphitic carbon nitride. Adv. Mater. 27 (13), 2150–2176.

Cao, S., Zhou, N., Gao, F., Chen, H., Jiang, F., 2017. All-solid-state Z-scheme 3, 4-dihydroxybenzaldehyde-functionalized Ga_2O_3/graphitic carbon nitride photocatalyst with aromatic rings as electron mediators for visible-light photocatalytic nitrogen fixation. Appl. Catal. B Environ. 218, 600–610.

Chai, C., Fan, C., Liu, J., Zhang, X., Wang, Y., Li, R., Duan, D., Wang, Y., 2019. Photoinduced g–C_3N_4–promoted $Mn^{2+}/Mn^{3+}/Mn^{4+}$ redox cycles for activation of peroxymonosulfate. J. Solid State Chem. 277, 466–474.

Chan, K.H., Chu, W., 2009. Degradation of atrazine by cobalt-mediated activation of peroxymonosulfate: different cobalt counter anions in homogenous process and cobalt oxide catalysts in photolytic heterogeneous process. Water Res. 43, 2513–2521.

Chandel, N., Sharma, K., Sudhaik, A., Raizada, P., Bandegharaei, A.H., Thakur, V.K., Singh, P., 2019. Magnetically separable $ZnO/ZnFe_2O_4$ and $ZnO/CoFe_2O_4$ photocatalysts supported onto nitrogen doped graphene for photocatalytic degradation of toxic dyes. Arab. J. Chem. 13 (2), 4324–4340.

Chen, D., Xie, Z., Zeng, Y., Lv, W., Zhang, Q., Wang, F., Liu, G., Liu, H., 2019. Accelerated photocatalytic degradation of quinolone antibiotics over Z-scheme MoO_3/g-C_3N_4 heterostructure by peroxydisulfate under visible light irradiation: mechanism; kinetic; and products. J. Taiwan Inst. Chem. Eng. 104, 250–259.

Chen, X., Oh, W.D., Lim, T.T., 2018. Graphene-and CNTs-based carbocatalysts in persulfates activation: material design and catalytic mechanisms. Chem. Eng. J. 354, 941–976.

Dikdim, J.M., Gong, Y., Noumi, G.B., Sieliechi, J.M., Zhao, X., Ma, N., Yang, M., Tchatchueng, J.B., 2019. Peroxymonosulfate improved photocatalytic degradation of atrazine by activated carbon/graphitic carbon nitride composite under visible light irradiation. Chemosphere 217, 833–842.

Dominguez, D., Gujer, W., 2006. Evolution of a wastewater treatment plant challenges traditional design concepts. Water Res. 40 (7), 1389–1396.

Dong, G., Zhang, Y., Pan, Q., Qiu, J., 2014. A fantastic graphitic carbon nitride (g-C_3N_4) material: electronic structure, photocatalytic and photoelectronic properties. J. Photochem. Photobiol. C 20, 33–50.

Dong, L., Xu, T., Chen, W., Lu, W., 2019. Synergistic multiple active species for the photocatalytic degradation of contaminants by imidazole-modified g-C_3N_4 coordination with iron phthalocyanine in the presence of peroxymonosulfate. Chem. Eng. J. 357, 198–208.

Dou, M., Wang, J., Gao, B., Ma, Z., Huang, X., 2020. A novel in-situ chemical oxidation channel-selective pH-dependence of refractory β-lactam antibiotics in the synergistic mechanism of persulfate and g-C_3N_4 under visible light. Chem. Eng. J. 394, 124899.

Du, X., Bai, X., Xu, L., Yang, L., Jin, P., 2020. Visible-light activation of persulfate by TiO_2/g-C_3N_4 photocatalyst toward efficient degradation of micropollutants. Chem. Eng. J. 384, 123245.

Duan, X., Sun, H., Kang, J., Wang, Y., Indrawirawan, S., Wang, S., 2015. Insights into heterogeneous catalysis of persulfate activation on dimensional-structured nanocarbons. ACS Catal. 5, 4629–4636.

Dutta, V., Singh, P., Shandilya, P., Sharma, S., Raizada, P., Saini, A.K., Gupta, V.K., Bandegharaei, A.H., Agarwal, S., Rahmani, A.S., 2019. Review on advances in photocatalytic water disinfection utilizing graphene and graphene derivatives-based nanocomposites. J. Environ. Chem. Eng. 7 (3), 103132.

Fang, J.Y., Shang, C., 2012. Bromate formation from bromide oxidation by the UV/persulfate process. Environ. Sci. Technol. 46, 8976–8983.

Fronczak, M., 2020. Adsorption performance of graphitic carbon nitride-based materials: current state of the art. J. Environ. Chem. Eng. 8 (5), 104411.

Ghanbari, F., Moradi, M., 2017. Application of peroxymonosulfate and its activation methods for degradation of environmental organic pollutants: review. Chem. Eng. J. 310, 41–62.

Gong, Y., Zhao, X., Zhang, H., Yang, B., Xiao, K., Guo, T., Zhang, J., Shao, H., Wang, Y., Yu, G., 2018. MOF-derived nitrogen doped carbon modified g-C_3N_4 heterostructure composite with enhanced photocatalytic activity for bisphenol A degradation with peroxymonosulfate under visible light irradiation. Appl. Catal. B Environ. 233, 35–45.

Guo, F., Lu, J., Liu, Q., Zhang, P., Zhang, A., Cai, Y., Wang, Q., 2018. Degradation of Acid Orange 7 by peroxymonosulfate activated with the recyclable nanocomposites of g-C_3N_4 modified magnetic carbon. Chemosphere 205, 297–307.

Hasija, V., Sharma, K., Kumar, V., Sharma, S., Sharma, V., 2018. Green synthesis of agar/Gum Arabic based superabsorbent as an alternative for irrigation in agriculture. Vacuum 157, 458–464.

Hasija, V., Raizada, P., Thakur, V.K., Khan, A.A.P., Asiri, A.M., Singh, P., 2020. An overview of strategies for enhancement in photocatalytic oxidative ability of MoS_2 for water purification. J. Environ. Chem. Eng. 8, 104307.

Hu, L., Deng, G., Lu, W., Lu, Y., Zhang, Y., 2017. Peroxymonosulfate activation by Mn_3O_4/metal-organic framework for degradation of refractory aqueous organic pollutant rhodamine B. Chin. J. Catal. 38, 1360–1372.

Hu, L., Wang, P., Shen, T., Wang, Q., Wang, X., Xu, P., Zheng, Q., Zhang, G., 2020. The application of microwaves in sulfate radical-based advanced oxidation processes for environmental remediation: a review. Sci. Total Environ. 722, 137831.

Jiang, W., Luo, W., Wang, J., Zhang, M., Zhu, Y., 2016. Enhancement of catalytic activity and oxidative ability for graphitic carbon nitride. J. Photochem. Photobiol. C 28, 87–115.

Jiang, X., Li, J., Fang, J., Gao, L., Cai, W., Li, X., Xu, A., Ruan, X., 2017. The photocatalytic performance of g-C_3N_4 from melamine hydrochloride for dyes degradation with peroxymonosulfate. J. Photochem. Photobiol. A: Chem. 336, 54–62.

Jin, C., Wang, M., Li, Z., Kang, J., Zhao, Y., Han, J., Wu, Z., 2020. Two dimensional Co_3O_4/g-C_3N_4 Z-scheme heterojunction: mechanism insight into enhanced peroxymonosulfate-mediated visible light photocatalytic performance. Chem. Eng. J. 398, 125569.

Jin, C., Kang, J., Li, Z., Wang, M., Wu, Z., Xie, Y., 2020. Enhanced visible light photocatalytic degradation of tetracycline by MoS_2/Ag/g-C_3N_4 Z-scheme composites with peroxymonosulfate. Appl. Surf. Sci. 514, 146076.

Jourshabani, M., Lee, B.K., Shariatinia, Z., 2020. From traditional strategies to Z-scheme configuration in graphitic carbon nitride photocatalysts: recent progress and future challenges. Appl. Catal. B: Environ. 276, 119157.

Kumar, A., Raizada, P., Bandegharaei, A.H., Thakur, V.K., Nguyen, V.H., Singh, P., 2021. C-, N-vacancy defect engineered polymeric carbon nitride towards photocatalysis: viewpoints and challenges. J. Mater. Chem. A 9, 111–1153.

Lan, Y., Li, Z., Li, D., Xie, W., Yan, G., Guo, S., 2020. Visible-light responsive Z-scheme Bi@β-Bi_2O_3/g-C_3N_4 heterojunction for efficient photocatalytic degradation of 2, 3-dihydroxynaphthalene. Chem. Eng. J. 392 (2020), 123686.

Lee, J., Gunten, U.V., Kim, J.H., 2020. Persulfate-based advanced oxidation: critical assessment of opportunities and roadblocks. Environ. Sci. Technol. 54 (6), 3064–3081.

Lee, J., Gunten, U.V., Kim, J.H., 2020. Persulfate-based advanced oxidation: critical assessment of opportunities and roadblocks. Environ. Sci. Technol. 54 (6), 3064–3081.

Li, J., Fang, J., Ye, P., Wu, D., Wang, M., Li, X., Xu, A., 2017. Peroxymonosulfate activation by iron oxide modified g-C_3N_4 under visible light for pollutants degradation. J. Photochem. Photobiol. A: Chem. 342, 85–93.

Li, Y., Yang, T., Qiu, S., Lin, W., Yan, J., Fan, S., Zhou, Q., 2020. Uniform N-coordinated single-atomic iron sites dispersed in porous carbon framework to activate PMS for efficient BPA degradation via high-valent iron-oxo species. Chem. Eng. J. 389, 124382.

Lin, Y., Shi, H., Jiang, Z., Wang, G., Zhang, X., Zhu, H., Zhang, R., Zhu, C., 2017. Enhanced optical absorption and photocatalytic H_2 production activity of g-C_3N_4/TiO_2 heterostructure by interfacial coupling: a DFT+ U study. Int. J. Hydrog. Energy 42, 9903–9913.

Liu, B., Qiao, M., Wang, Y., Wang, L., Gong, Y., Guo, T., Zhao, X., 2017. Persulfate enhanced photocatalytic degradation of bisphenol A by g-C_3N_4 nanosheets under visible light irradiation. Chemosphere 189, 115–122.

Liu, B., Song, W., Wu, H., Liu, Z., Teng, Y., Sun, Y., Xu, Y., Zheng, H., 2020. Degradation of norfloxacin with peroxymonosulfate activated by nanoconfinement Co_3O_4@ CNT nanocomposite. Chem. Eng. J. 398, 125498.

Liu, J., Cheng, B., Yu, J., 2016. A new understanding of the photocatalytic mechanism of the direct Z-scheme gC_3N_4/TiO_2 heterostructure. Phys. Chem. Chem. Phys. 18, 31175–31183.

Liu, W., Zhou, J., Yao, J., 2020. Shuttle-like CeO_2/g-C_3N_4 composite combined with persulfate for the enhanced photocatalytic degradation of norfloxacin under visible light. Ecotoxicol. Environ. Saf. 190, 110062.

Ma, D., Wu, J., Gao, M., Xin, Y., Chai, C., 2017. Enhanced debromination and degradation of 2, 4-di-bromophenol by Z-scheme Bi_2MoO_6/CNTs/g-C_3N_4 visible light photocatalyst. Chem. Eng. J. 316, 461–470.

Ma, R., Zhou, Y., Bi, H., Yang, M., Wang, J., Liu, Q., Huang, F., 2020. Multidimensional graphene structures and beyond: unique properties, syntheses and applications. Prog. Mater. Sci. 113, 100665.

Mamba, G., Mishra, A., 2016. Graphitic carbon nitride (g-C_3N_4) nanocomposites: a new and exciting generation of visible light driven photocatalysts for environmental pollution remediation. Appl. Catal. B Environ. 198, 347–377.

Matzek, L.W., Carter, K.E., 2016. Activated persulfate for organic chemical degradation: a review. Chemosphere 151, 178–188.

Miklos, D.B., Remy, C., Jekel, M., Linden, K.G., Drewes, J.E., Hubner, U.J., 2018. Evaluation of advanced oxidation processes for water and wastewater treatment–a critical review. Water Res. 139, 118–131.

Nguyen, V.N., Nguyen, B.S., Jin, Z., Shokouhimehr, M., Jang, H.W., Hu, C., Singh, P., Raizada, P., Peng, W., Lam, S.S., Xia, C., Nguyen, C.C., Kim, S.Y., Le, Q.V., 2020. Towards artificial photosynthesis: sustainable hydrogen utilization for photocatalytic reduction of CO_2 to high-value renewable fuels. Chem. Eng. J. 402, 126184.

Oh, W.D., Dong, Z., Lim, T.T., 2016. Generation of sulfate radical through heterogeneous catalysis for organic contaminants removal: current development, challenges and prospects. Appl. Catal. B Environ. 194, 169–201.

Opoku, F., Govender, K.K., van Sittert, C.G.C.E., Govender, P.P., 2018. Insights into the photocatalytic mechanism of mediator-free direct Z-scheme g-C_3N_4/Bi_2MoO_6 (010) and g-C_3N_4/Bi_2WO_6 (010) heterostructures: a hybrid density functional theory study. Appl. Surf. Sci. 427, 487–498.

Patial, S., Hasija, V., Raizada, P., Singh, P., Singh, A.A., Asiri, A.M., 2020. Tunable photocatalytic activity of $SrTiO_3$ for water splitting: strategies and Future scenario. J. Environ. Chem. Eng. 8 (3), 103791.

Qi, K., Liu, S., Zada, A., 2020. Graphitic carbon nitride, a polymer photocatalyst. J. Taiwan Inst. Chem. Eng. 109, 111–123.

Qiao, M., Wu, X., Zhao, S., Djellabi, R., Zhao, X., 2020. Peroxymonosulfate enhanced photocatalytic decomposition of silver-cyanide complexes using g-C_3N_4 nanosheets with simultaneous recovery of silver. Appl. Catal. B: Environ. 265, 118587.

Raizada, P., Sudhaik, A., Singh, V.P., Gupta, V.K., Bandegharaei, A.H., Kumar, R., Singh, P., 2019. Solar light assisted degradation of oxytetracycline from water using Bi_2O_3/Fe_3O_4 supported graphitic carbon nitride photocatalyst. Desalin. Water Treat. 148, 338–350.

Raizada, P., Sudhaik, A., Singh, P., Bandegharaei, A.H., Thakur, P., 2019. Converting type II AgBr/VO into ternary Z scheme photocatalyst via coupling with phosphorus doped g-C_3N_4 for enhanced photocatalytic activity. Sep. Purif. Technol. 227, 115692.

Raizada, P., Sudhaik, A., Singh, P., Shandilya, P., Saini, A.K., Gupta, V.K., Lim, J., Jung, H., Hosseini, A., 2019. Fabrication of Ag_3VO_4 decorated phosphorus and sulphur co-doped graphitic carbon nitride as a high-dispersed photocatalyst for phenol mineralization and E. coli disinfection. Sep. Purif. Technol. 212, 887–900.

Raizada, P., Sudhaik, A., Singh, P., Shandilya, P., Thakur, P., Jung, H., 2020. Visible light assisted photodegradation of 2, 4-dinitrophenol using Ag_2CO_3 loaded phosphorus and sulphur co-doped graphitic carbon nitride nanosheets in simulated wastewater. Arab. J. Chem. 13 (1), 3196–3209.

Reddy, E.P., Davydov, L., Smirniotis, P., 2003. TiO_2-loaded zeolites and mesoporous materials in the sono-photocatalytic decomposition of aqueous organic pollutants: the role of the support. Appl. Catal. B Environ. 42 (1), 1–11.

Ren, Y., Zeng, D., Ong, W.J., 2019. Interfacial engineering of graphitic carbon nitride (g-C_3N_4)-based metal sulfide heterojunction photocatalysts for energy conversion: a review. Chin. J. Catal. 40 (3), 289–319.

Rojas, G.G., Saucedo, F.L., Bucio, E., 2020. Gamma-irradiation applied in the synthesis of metallic and organic nanoparticles: a short review. Radiat. Phys. Chem. 169, 107962.

Sano, T., Sato, H., Hori, T., Hirakawa, T., Teramoto, Y., Koike, K., 2019. Effects of polymeric-and electronic-structure of graphitic carbon nitride (g-C_3N_4) on oxidative photocatalysis. Mol. Catal. 474, 110451.

Shao, H., Zhao, X., Wang, Y., Mao, R., Wang, Y., Qiao, M., Zhao, S., Zhu, Y., 2017. Synergetic activation of peroxymonosulfate by Co_3O_4 modified g-C_3N_4 for enhanced degradation of diclofenac sodium under visible light irradiation. Appl. Catal. B Environ. 218, 810–818.

Singh, P., Sharma, K., Hasija, V., Sharma, V., Sharma, S., Raizada, P., Thakur, V.K., 2019. Systematic review on applicability of magnetic iron oxides–integrated photocatalysts for degradation of organic pollutants in water. Mater. Today Chem. 14, 100–186.

Song, Y., Huang, L., Zhang, X., Zhang, H., Wang, L., Zhang, H., Liu, Y., 2020. Synergistic effect of persulfate and g-C_3N_4 under simulated solar light irradiation: implication for the degradation of sulfamethoxazole. J. Hazard. Mater. 393, 122379.

Sonu, Dutta, V., Sharma, S., Raizada, P., Bandegharaei, A.H., Gupta, V.K., Singh, P., 2019. Review on augmentation in photocatalytic activity of $CoFe_2O_4$ via heterojunction formation for photocatalysis of organic pollutants in water. J. Saudi Chem. Soc. 23 (8), 1119–1136.

Stelo, F., Kublik, N., Ullah, S., Wender, H., 2020. Recent advances in Bi_2MoO_6 based Z-scheme heterojunctions for photocatalytic degradation of pollutants. J. Alloy. Compd. 829, 154591.

Sudhaik, A., Raizada, P., Shandilya, P., Jeong, D., Lim, J., Singh, P., 2018. Review on fabrication of graphitic carbon nitride based efficient nanocomposites for photodegradation of aqueous phase organic pollutants. J. Ind. Eng. Chem. 68, 28–51.

Tao, Y., Ni, Q., Wei, M., Xia, D., Li, X., Xu, A., 2015. Metal-free activation of peroxymonosulfate by g-C_3N_4 under visible light irradiation for the degradation of organic dyes. RSC Adv. 5 (55), 44128–44136.

Valerio, A., Wang, J., Tong, S., Souza, A.A.U., Hotza, D., Gonzalez, S.Y.G., 2020. Synergetic effect of photocatalysis and ozonation for enhanced tetracycline degradation using highly macroporous photocatalytic supports. Chem. Eng. Process. - Process Intensif. 149, 107838.

Wang, J., Wang, S., 2018. Activation of persulfate (PS) and peroxymonosulfate (PMS) and application for the degradation of emerging contaminants. Chem. Eng. J. 334, 1502–1517.

Wang, J., Hong, G., Yang, L., Wei, L., Yang, B., 2020. Peroxymonosulfate activation by porous $BiFeO_3$ for the degradation of bisphenol AF: non-radical and radical mechanism. Appl. Surf. Sci. 507, 145097.

Wang, X., Wang, A., Ma, J., 2017. Visible-light-driven photocatalytic removal of antibiotics by newly designed C_3N4@ $MnFe_2O_4$-graphene nanocomposites. J. Hazard. Mater. 336, 81–92.

Wang, Y., Hui, S., Zhan, S., Djellabi, R., Li, J., Zhao, X., 2020. Activation of peroxymonosulfate by novel Pt/Al_2O_3 membranes via a nonradical mechanism for efficient degradation of electron-rich aromatic pollutants. Chem. Eng. J. 381, 122563.

Wang, Z., Sun, L., Lou, X., Yang, F., Feng, M., Liu, J., 2017. Chemical instability of graphene oxide following exposure to highly reactive radicals in advanced oxidation processes. J. Colloid Interface Sci. 507, 51–58.

Wardman, P., 1989. Reduction potentials of one electron couples involving free radicals in aqueous solution. J. Phys. Chem. Ref. Data 18, 1637–1755.

Wu, F., Huang, H., Xu, T., Lu, W., Li, N., Chen, W., 2017. Visible-light-assisted peroxymonosulfate activation and mechanism for the degradation of pharmaceuticals over pyridyl-functionalized graphitic carbon nitride coordinated with iron phthalocyanine. Appl. Catal. B Environ. 218, 230–239.

Xiao, R., Luo, Z., Wei, Z., Luo, S., Spinney, R., Yang, W., Dionysiou, D.D., 2018. Activation of peroxymonosulfate/persulfate by nanomaterials for sulfate radical-based advanced oxidation technologies. Curr. Opin. Chem. Eng. 19, 51–58.

Xiao, R., Liu, K., Bai, L., Minakata, D., Seo, Y., Goktaş, R.K., Dionysiou, D.D., Tang, C.J., Wei, Z., Spinney, R., 2019. Inactivation of pathogenic microorganisms by sulfate radical: present and future. Chem. Eng. J. 371, 222–232.

Xu, L., Qi, L., Sun, Y., Gong, H., Chen, Y., Pei, C., Gan, L., 2020. Mechanistic studies on peroxymonosulfate activation by g-C_3N_4 under visible light for enhanced oxidation of light-inert dimethyl phthalate. Chin. J. Catal. 41 (2), 322–332.

Xue, W., Huang, D., Wen, X., Chen, S., Cheng, M., Deng, R., Li, B., Yang, Y., Liu, X., 2020. Silver-based semiconductor Z-scheme photocatalytic systems for environmental purification. J. Hazard. Mater. 390, 122128.

Yang, L., Bai, X., Shi, J., Du, X., Xu, L., Jin, P., 2019. Quasi-full-visible-light absorption by D35-TiO_2/g-C_3N_4 for synergistic persulfate activation towards efficient photodegradation of micropollutants. Appl. Catal. B: Environ. 256, 117759.

Yang, S., Wang, P., Yang, X., Shan, L., Zhang, W., Shao, X., Niu, R., 2010. Degradation efficiencies of azo dye Acid Orange 7 by the interaction of heat, UV and anions with common oxidants: persulfate, peroxymonosulfate and hydrogen peroxide. J. Hazard. Mater. 179, 552–558.

Ye, P., Wu, D., Wang, M., Wei, Y., Xu, A., Li, X., 2018. Coating magnetic $CuFe_2O_4$ nanoparticles with OMS-2 for enhanced degradation of organic pollutants via peroxymonosulfate activation. Appl. Surf. Sci. 428, 131–139.

Yi, H., Huang, D., Zeng, G., Lai, C., Qin, L., Cheng, M., Ye, S., Song, B., Ren, X., Guo, X., 2018. Selective prepared carbon nanomaterials for advanced photocatalytic application in environmental pollutant treatment and hydrogen production. Appl. Catal. B Environ. 239, 408–424.

Yi, J., Alami, W.E., Song, Y., Li, H., Ajayan, P.M., Xu, H., 2020. Emerging surface strategies on graphitic carbon nitride for solar driven water splitting. Chem. Eng. J. 382, 122812.

Yin, R., Guo, W., Wang, H., Du, J., Zhou, X., Wu, Q., Zheng, H., Chang, J., Ren, N., 2018. Enhanced peroxymonosulfate activation for sulfamethazine degradation by ultrasound irradiation: performances and mechanisms. Chem. Eng. J. 335, 145–153.

Yu, J., Feng, H., Tang, L., Pang, Y., Zeng, G., Lu, Y., Dong, H., Wang, J., Liu, Y., Feng, C., Wang, J., Peng, B., Ye, S., 2020. Metal-free carbon materials for persulfate-based advanced oxidation process: microstructure, property and tailoring. Prog. Mater. Sci. 111, 100654.

Zeng, H., Zhang, H., Deng, L., Shi, Z., 2020. Peroxymonosulfate-assisted photocatalytic degradation of sulfadiazine using self-assembled multi-layered CoAl-LDH/g-C_3N_4 heterostructures: performance, mechanism and eco-toxicity evaluation. J. Water Process Eng. 33, 101084.

Zhang, J., Zhao, X., Wang, Y., Gong, Y., Cao, D., Qiao, M., 2018. Peroxymonosulfate-enhanced visible light photocatalytic degradation of bisphenol A by perylene imide-modified g-C_3N_4. Appl. Catal. B Environ. 237, 976–985.

Zhou, J., Liu, W., Cai, W., 2019. The synergistic effect of Ag/AgCl@ ZIF-8 modified g-C_3N_4 composite and peroxymonosulfate for the enhanced visible-light photocatalytic degradation of levofloxacin. Sci. Total Environ. 696, 133962.

Zhou, P., Peng, Huo, X., Zhang, J., Liu, Y., Cheng, F., Cheng, X., Wang, Y., Zhang, Y., 2020. Visible light induced acceleration of Fe (III)/Fe (II) cycles for enhancing phthalate degradation in C_{60} fullerenol modified Fe (III)/peroxymonosulfate process. Chem. Eng. J. 387, 124126.

Zhu, B., Cheng, B., Zhang, L., Yu, J., 2019. Review on DFT calculation of s-triazine-based carbon nitride. Carbon 1, 32–56.

Zhu, J., Xiao, P., Li, H., Carabineiro, S., 2014. Graphitic carbon nitride: synthesis, properties, and applications in catalysis. Appl. Mater. Interfaces 6, 6–19.

Zuo, S., Chen, Y., Liu, W., Yao, C., Li, X., Li, Z., Ni, C., Liu, X., 2017. A facile and novel construction of attapulgite/Cu_2O/Cu/g-C_3N_4 with enhanced photocatalytic activity for antibiotic degradation. Ceram. Int. 43, 3324–3329.

SUPPLEMENTARY MATERIAL

Advanced activation of persulfate by heterojunction polymeric graphitic carbon nitride (g-C_3N_4) based photocatalysts for environmental remediation: A review

Vasudha Hasija[a], Ajay Kumar[b], Pankaj Raizada[a], Venkata Krishnan[b], Aftab Aslam Parwaz Khan[c,d], Pardeep Singh[a,*], Eric Lichtfouse[e,f], Chuanyi Wang[g], Van-Huy Nguyen[h]

[a]School of Chemistry, Faculty of Basic Sciences, Shoolini University, Solan (HP), India--173229

[b]School of Basic Sciences and Advanced Materials Research Center, Indian Institute of Technology Mandi, Kamand, Mandi 175075, Himachal Pradesh, India.

[c]Center of Excellence for Advanced Materials Research, King Abdulaziz University, P.O.Box 80203, Jeddah,21589, Saudi Arabia

[d]Chemistry Department, Faculty of Science, King Abdulaziz University,P.O.Box 80203, Jeddah, Saudi Arabia

[e]Aix-Marseille Univ, CNRS, IRD, INRA, Coll France, CEREGE, Aix-en-Provence 13100, France

[f]International Research Centre for Renewable Energy, State Key Laboratory of Multiphase Flow in Power Engineering, Xi'an Jiaotong University, Xi'an, PR China

[g]School of Environmental Science and Engineering, Shaanxi University of Science and Technology, Xi'an 710021, PR China

[h]Institute of Research and Development, Duy Tan University, Da Nang 550000, Vietnam

Corresponding author: pardeepchem@gmail.com (Pardeep Singh)

Table S-1. Oxidation potential and reactions of different oxidants.

No.	Oxidant	Oxidation potential (V)	Reactive species	Reaction/pH
1	Hydroxyl	2.8	$OH^{\bullet}$	$OH^{\bullet} + H^{+} + e^{-} \rightarrow H_2O$ (Acidic) $OH^{\bullet} + e^{-} \rightarrow OH^{-}$ (Alkaline)
2	Sulfate	2.5-3.1	$SO_4^{\bullet-}$	$SO_4^{\bullet-} + e^{-} \rightarrow SO_4^{2-}$ (Acidic/neutral)
3	Peroxydisulfate	2.08	$S_2O_8^{2-}$, $OH^{\bullet}$, $SO_4^{\bullet-}$	$S_2O_8^{2-} + 2e^{-} \rightarrow 2SO_4^{2-}$ (Acidic)
4	Ozone	2.07	O_3	$O_3 + 2H^{+} + 2e^{-} \rightarrow O_2 + H_2O$ (Acidic) $O_3 + H_2O + 2e^{-} \rightarrow O_2 + 2OH^{-}$ (Alkaline)
5	Peroxymonosulfate	1.82	HSO_5^{-}	$HSO_5^{-} + H^{+} + 2e^{-} \rightarrow SO_4^{2-} + H_2O$ (Acidic)
6	Hydrogen peroxide	1.77	H_2O_2	$H_2O_2 + 2H^{+} + 2e^{-} \rightarrow 2H_2O$ (Acidic) $HO_2^{-} + H_2O + 2e^{-} \rightarrow 3OH^{-}$ (Alkaline)
7	Permanganate	1.68	MnO_4^{-}	$MnO_4^{-} + 4H^{+} + 3e^{-} \rightarrow MnO_2 + 2H_2O$ (Acidic) $MnO_4^{-} + 2H_2O + 3e^{-} \rightarrow MnO_2 + 4OH^{-}$ (Alkaline)
8	Chlorine	1.36	Cl^{-}	$Cl_2 + 2e^{-} \rightarrow 2Cl^{-}$ (Acidic)

Table S-2. PS/PMS photoactivation via pristine g-C_3N_4 for pollutant degradation.

No.	Photoactivation system	Pollutants	Reaction conditions	Wavelength of light used	Dominant reactive species	Degradation efficiency/ Reaction time	Ref.
1	g-C_3N_4 /PDS/Vis	β-lactam antibiotics i.e. amoxicillin (AMX), cefotaxime (CFX), meropenem (MER), sulbactam (SUL)	L.S; [β-lactam antibiotics] = 2 ppm/100 mL, [g-C_3N_4]= 1 g L^{-1}, [PDS]= 0.01 mM, pH = 7.	420 nm	$SO_4^{\bullet-}$ and $OH^{\bullet}$	99%, 60 min.	[60]
2	g-C_3N_4 /PDS/Vis	Bisphenol A (BPA)	L.S; 150 W Xe lamp, [BPA]= 5 mg L^{-1}, [g-C_3N_4] = 0.5 g L^{-1}, [PDS]= 5 mM, pH = 3.	400 nm	$SO_4^{\bullet-}$, $OH^{\bullet}$ and $O_2^{\bullet-}$	100%, 90 min	[61]
3	g-C_3N_4 /PDS/UV	Sulfamethoxazole (SMX)	L.S; 300 W Xe lamp, [SMX]= 10.0 μM, [g-C_3N_4] = 0.05 g L^{-1}, [PDS]= 0.5 mM, pH =7.6.	265 nm	$O_2^{\bullet-}$, h^+ and $SO_4^{\bullet-}$	98.4%, 60 min	[62]
4	g-C_3N_4 /PMS/Vis	Dimethyl phthalate (DMP)	L.S; LED, [DMP]=0.01 mM, [g-C_3N_4] = 0.5 g L^{-1}, [PMS]= 5.0 mM, pH= 2.5	420 nm	$SO_4^{\bullet-}$ and $OH^{\bullet}$	90%, 120 min	[63]
5	g-C_3N_4 /PMS/Vis	Acidic orange 7 (AO7) dye	L.S; 500 W Xe lamp, [AO7] = 20 mg L^{-1}, [g-C_3N_4] =0.4 g L^{-1}, [PMS]= 0.4 g L^{-1}, pH=3.83.	485 nm	$SO_4^{\bullet-}$ and $O_2^{\bullet-}$	86%, 30 min	[64]

6	g-C_3N_4 /PMS/Vis	Acidic orange 7 (AO7) dye	L.S; 500 W Xe lamp, [AO7] = 20mg L^{-1}, [g-C_3N_4] = 0.4 g L^{-1}, [PMS]= 0.2 g L^{-1}, pH=11.7.	420 nm	$O_2^{\bullet -}$, h^+ and $SO_4^{\bullet -}$	100%, 30 min	[65]
7	g-C_3N_4 /PMS/Vis	Silver cyanide $[Ag(CN)_2]^-$	L.S; 300 W Xe lamp, $[Ag(CN)_2]^-$=0.45 mM, [g-C_3N_4] = 1.0 g L^{-1}, [PMS]= 0.5 mM, pH=10	400 nm	$O_2^{\bullet -}$, h^+, e^- and $SO_4^{\bullet -}$	74%, 150 min	[66]

L.S; light source, LED; light emitting diode, UV; ultraviolet, Vis; visible.

Table S-3. PS/PMS photoactivation via g-C_3N_4 heterostructures for pollutants degradation.

No.	Photoactivation system	Doping level	Pollutants	Reaction conditions	Wavelength of light used	BET (Bare g-C_3N_4 / Doped g-C_3N_4)	Dominant reactive species	Degradation efficiency/ Reaction time	Ref.
1	g-C_3N_4 /CeO_2/PDS/Vis	Type-II	Norfloxacin (NOR)	L.S; 150 W Xe lamp, [NOR] = 10 mg L^{-1}, [P.C] =1 g L^{-1}, [PDS] = 5 mM, pH = 8.5.	420 nm	-	$O_2^{\bullet -}$, $SO_4^{\bullet -}$ and $OH^{\bullet}$	88.6%, 60 min	[79]
2	D-35-TiO_2/g-C_3N_4 /PDS/Vis	Type-II	Bisphenol A(BPA)	L.S; 300 W Xe lamp, [BPA] =10 mg L^{-1}, [P.C] = 0.5 g L^{-1}, [PDS] = 2 mM, pH = 7.	675 nm	-	$SO_4^{\bullet -}$, $OH^{\bullet}$, $O_2^{\bullet -}$ and h	100%, 30 min	[80]
3	g-C_3N_4 /$MnFe_2O_4$/ graphene/PDS/Vis	Type-II	Metronidazole (MNZ), Amoxicillin (AMX), Tetracycline (TC), Ciprofloxacin (CIP)	L.S; 300 W Xe lamp, [MNZ], [AMX], [TC] = 20 mg L^{-1}, [CIP] = 10 mg L^{-1}, [P.C] = 1 mg mL^{-1}, [PDS] = 0.01 mol L^{-1}.	450 nm	-	$SO_4^{\bullet -}$ and $OH^{\bullet}$	91.5%, 60 min	[81]
4	CoAl-LDH/g-C_3N_4 /PMS/Vis	Type-II	Sulfadiazine (SDZ)	L.S; 100 W m^{-2}, [SDZ] = 10 μM, [P.C] = 0.2 g	450 nm	-	$SO_4^{\bullet -}$, $OH^{\bullet}$ and $O_2^{\bullet -}$	87.1%, 15 min	[82]

				L^{-1}, [PMS] = 0.5 mM, pH = 10.5.					
5	Activated carbon/g-C_3N_4 /PMS/Vis	Type-II	Atrazine (AZ)	L.S; 300 W Xe lamp, [AZ] = 5 mg L^{-1}, [P.C] = 1 g L^{-1}, [PMS] = 5 mM, pH = 5.56.	465 nm	g-C_3N_4; 73 m^2/g, AC/g-C_3N_4; 112 m^2/g	$SO_4^{\bullet-}$ and $OH^{\bullet}$	98.7%, 120 min	[83]
6	Fe_2O_3/g-C_3N_4/ PMS/Vis	Type-II	Acidic orange 7 (AO7) dye	L.S; 500 W Xe lamp, [AO7] = 20 mg L^{-1}, [P.C] = 0.4 g L^{-1}, [PMS] = 0.2 g L^{-1}.	420 nm	g-C_3N_4; 30m^2/g, Fe_2O_3/g-C_3N_4; 97 m^2/g	$SO_4^{\bullet-}$, $OH^{\bullet}$ and h^+	98.5%, 20 min	[84]
7	g-C_3N_4/Mn_3O_4/ PMS/Vis	Type-II	Phenol	L.S; 300 W Xe lamp, [Phenol] = 20 mg L^{-1}, [P.C] = 0.2 g L^{-1}, [PMS] = 0.6 g L^{-1}, pH = 7.	420 nm	-	$SO_4^{\bullet-}$ and $OH^{\bullet}$	87.3%, 60 min	[85]
8	TiO_2/g-C_3N_4/ PDS/Vis	Type-II	Acetaminophen (AAP)	L.S; 300 W Xe lamp, [AAP] = 5mg L^{-1}, [P.C] = 0.5 g L^{-1}, [PDS] = 2 mM, pH = 7	400 nm	-	$SO_4^{\bullet-}$, $OH^{\bullet}$ and h^+	82.5%, 60 min	[86]
9	Fe_3O_4@C/g-C_3N_4/ PMS/Vis	Type-II	Acidic orange 7 (AO7)	L.S; 350 W Xe lamp, [AO7] = 20 mg L^{-1}, [P.C] = 0.6 g L^{-1}, [PMS] = 0.1 g L^{-1}, pH = 2	484 nm	-	$SO_4^{\bullet-}$ and $OH^{\bullet}$	97%, 40 min	[87]

10	N-doped ZIF-8/g-C_3N_4/PMS/Vis	Type -II	Bisphenol A (BPA)	L.S; 300 W Xe lamp, [BPA] = 20 mg L^{-1}, [P.C] = 0.5 g L^{-1}, [PMS] = 2.0 mM, pH = 11.0.	400 nm	-	$SO_4^{\bullet -}$ and $OH^{\bullet}$	97%, 60 min	[88]
11	MoS_2/Ag/g-C_3N_4 /PMS/Vis	ASS	Tetracycline (TC)	L.S; 350 W Xe lamp, [TC] = 20 mg L^{-1}, [P.C] = 0.2 g L^{-1}, [PMS] = 0.1 mM, pH = 5.5.	420 nm	g-C_3N_4; 43.2 m^2/g, MoS_2/Ag/ g-C_3N_4; 50.2 m^2/g	$SO_4^{\bullet -}$, $OH^{\bullet}$ and $O_2^{\bullet -}$	98.9 %, 50 min	[90]
12	Ag/AgCl@ZIF-8/g-C_3N_4/PMS/Vis	ASS	Levofloxacin (LVFX)	L.S; 150 W Xe lamp, [LVFX]= 10 mg L^{-1}, [P.C] = 0.1 g L^{-1}, [PMS] = 2 mM, pH = 9	450 nm	-	$O_2^{\bullet -}$, $SO_4^{\bullet -}$ and $OH^{\bullet}$	87.5%, 60 min	[91]
13	Perylene imide/g-C_3N_4/PMS/Vis	Direct Z-scheme	Bisphenol A (BPA)	L.S; 300 W Xe lamp, [BPA] = 10 mg L^{-1}, [Cat]= 1 g L^{-1}, [PMS] = 5 mM, pH = 11.0	400 nm	g-C_3N_4; 15.4 m^2/g, PI/g-C_3N_4 = 21.6 m^2/g	$SO_4^{\bullet -}$ and $OH^{\bullet}$	96%, 60 min	[95]
14	g-C_3N_4 /Co_3O_4/ PMS/Vis	Direct Z-scheme	Diclofenac (DCF)	L.S; 300 W Xe lamp, [DCF] = 10 mg L^{-1}, [P.C] = 0.5 g L^{-1}, [PMS] = 0.1 mM, pH = 6.7.	420 nm	-	$SO_4^{\bullet -}$, $OH^{\bullet}$	100%, 30 min	[96]
15	g-C_3N_4 -INA (isonicotinic acid)- $FePcCl_{16}$/	Direct Z-scheme	Carbamazepine (CBZ)	L.S; 300 W Xe lamp,	420 nm	-	$SO_4^{\bullet -}$, $OH^{\bullet}$	94%, 40 min	[97]

	PMS/Vis			[CBZ] = 25 µM, [P.C] = 0.1 g L^{-1}, [PMS] = 0.18 mM, pH = 5.					
16	$g\text{-}C_3N_4$ -IMA (imidazole)-$FePcCl_{16}$/PMS	Direct Z-scheme	Carbamazepine (CBZ)	L.S; 350 W Xe lamp, [CBZ] = 25 µM, [P.C] = 0.1 g L^{-1}, [PMS] = 0.3 mM, pH = 7	420 nm	-	$SO_4^{\bullet-}$, $OH^{\bullet}$	95%, 25 min	[98]

L.S; light source, P.C; photocatalyst, AAS; All solid state.

1.1. PMS and PDS as sulphate radical source

The PDS is a white or colourless crystal commonly available as potassium PDS ($K_2S_2O_8$) or sodium PDS ($Na_2S_2O_8$) with high thermal stability [1]. It has a water solubility of 750 g·L^{-1} and forms an acidic solution in water. The symmetrical structure of PDS ($^-O_3SO_3\text{-}OSO_3^-$) has peroxo (O-O) bond length of 1.497 Å with 140 kJ·mol^{-1} bond energy [2, 3]. The storage and transport of solid PDS and PMS are more accessible as compared to H_2O_2 and O_3. PDS is a strong oxidizer with a 2.01 V potential that allows its activation in UV irradiation at 254 nm to generate $SO_4^{\bullet-}$ radical, which on further reaction with H_2O molecules or under alkaline conditions produces $OH^{\bullet}$ and $O_2^{\bullet-}$ radicals, respectively, as shown in Eqs. [1-3]

$$S_2O_8^{2-} + h\vartheta \rightarrow 2SO_4^{\bullet-} \qquad (1)$$

$$SO_4^{-} + H_2O \rightarrow SO_4^{-2} + OH^{\cdot} \qquad (2)$$

$$2S_2O_8^{2-} + 4OH^{-} \rightarrow SO_4^{\bullet-} + 3SO_4^{2-} + O_2^{\bullet-} + 2H_2O \qquad (3)$$

The apparent quantum yield of $SO_4^{\bullet-}$ obtained by UV-activated PDS is higher than alkaline medium/base activated PDS [4]. Also, only one molecule of $S_2O_8^{2-}$ is required to generate two molecules of $SO_4^{\bullet-}$ whereas another molecule of $SO_4^{\bullet-}$ is derived through the nucleophilic attack by a base [5]. The inorganic chemical oxidant PMS is unsymmetrical ($^-O_3SO\text{-}OH$) with 1.453 Å O-O bond distance and bond energy of 140.0-213.3 $kJ\cdot mol^{-1}$ [6]. Anipsitakis and Dionysiou first introduced Peroxymonosulphate (PMS) in 2003 to degrade 2,4-dichlorphenol, atrazine, and naphthalene *via* cobalt-mediated PMS activation [7]. Since then, PMS has been widely explored as an alternative to chlorine-sanitizers and chlorine-based bleaching agents due to economic and commercial availability as Oxone® triple salt ($KHSO_5\cdot 0.5\ KHSO_4\cdot 0.5K_2SO_4$) [8]. PMS is highly soluble in water with a solubility of (>250 $g\cdot L^{-1}$) and forms an acidic water solution. PMS alkaline activation depends on pH values and undergoes interconversions between $SO_4^{\bullet-}$ and $OH^{\bullet}$ radicals [46]. The persulphate-based AOPs displays higher mineralization ability and a broader working pH range from 2 to 10 [9].

- At pH < 6 and pH = 12, it is most stable with $SO_4^{\bullet-}$ as the dominant radical.
- At pH = 9, PMS undergoes equimolar dissociation releasing both $SO_4^{\bullet-}$ and $OH^{\bullet}$ radicals.
- At pH > 9, PMS is hydrolysed into H_2O_2 with $OH^{\bullet}$ as the dominant reactive species.

The un-symmetric PMS generates one $SO_4^{\cdot-}$ and one $OH^{\cdot}$ under UV radiations [10], and the resultant $SO_4^{\bullet-}$ radical might react with H_2O to produce $OH^{\bullet}$ as described in eq. [4, 5] as follows;

$$HSO_5^- + h\vartheta \rightarrow SO_4^{\bullet-} + OH^{\cdot} \qquad (4)$$

$$SO_4^{\cdot-} + H_2O \rightarrow OH^{\cdot} + HSO_4^- \qquad (5)$$

Among the different photolysis processes, UV responsive photolysis is considered as an effective route for PMS/PDS activation [11]. The UV wavelength at 254 nm produced the highest quantum yields of 1.4 for $SO_4^{\bullet-}$ generation, but up to 351 nm, the quantum yield declined [12]. Thus, extended solar spectrum exposure, *i.e.,* visible region (400-460 nm) or even beyond, is preferred to design an energy-efficient PDS activation process [13]. Semiconductor heterogeneous photocatalysis for persulphate activation is highly preferred for the complete mineralization of refractory pollutants [14]**.** Typically, PMS/PDS photocatalytic activation proceeds *via* solar-driven electronic excitations in a photocatalyst (PC) with appropriate band potential capable of dissociating peroxo (O-O) bond in PMS/PDS to generate free radical activated complexes for mineralization of targeted pollutants [15].

1.2. Non-radical reactions in PMS/PDS

The metal free carbon catalysts (MFCCs) driven PMS/PDS non-radical processes [16] presented in [Fig. 2b] are three major reaction mechanisms for the catalytic oxidation of organic pollutants: (1) singlet oxygen ($^1O_2$): the PMS/PDS are converted by the carbon catalyst to a non-active oxidizing species [17]. $^1O_2$ is regarded as the non-radical species due to its milder oxidizing ability than $SO_4^{\bullet-}$ and $OH^{\bullet}$ [18]; (2) catalytic electron transfer: the contaminants transfer electrons to PMS/PDS to complete oxidative degradation of contaminants [19]; (3) charge transfer surface activated complexes: the PMS/PDS are activated on the surface of the catalyst into active molecules, and then oxidizes pollutants efficiently i.e.; surface-bound $SO_4^{\cdot-}$ radicals which is the metastable state of the activated PDS [20, 21]. These three non-radical reaction mechanisms are involved in the PMS/PDS activation.

Unlike radical pathway involving electron transfer between the catalyst and PDS, the nonradical pathways over carbon catalyst serves only as a platform for PDS and pollutant to react, allowing better preservation of the structural integrity of catalyst during oxidation reaction [22]. About the mechanism on the activation of PDS/PMS by carbon materials, it is generally accepted that PDS/PMS interacts with some active sites of carbon catalysts to form non-radical reactive molecules [23-25]. Although the non-radical reactions have been well-confirmed, the accurate mechanism PMS/PDS activation through non-radical pathways still remain controversial and requires more investigations**.**

References:

[1] Y. Zhang, B.T Zhang, Y. Teng, J. Zhao, X. Sun, Heterogeneous activation of persulfate by carbon nanofiber supported Fe_3O_4@ carbon composites for efficient ibuprofen degradation, J. Hazard. Mater. 401 (2021) 123428.

[2] X. Hou, G. Zhan, X. Huang, N. Wang, Z. Ai, L. Zhang, Persulfate activation induced by ascorbic acid for efficient organic pollutants oxidation, Chem. Eng. J. 382 (2020) 122355.

[3] J. Tan, Z. Li, J. Li, J. Wu, X. Yao, T. Zhang, Graphitic carbon nitride-based materials in activating persulfate for aqueous organic pollutants degradation: A review on materials design and mechanisms, Chemosphere 262 (2021) 127675.

[4] P. Devi, U. Das, A.K. Dalai, In-situ chemical oxidation: Principle and applications of peroxide and PS treatments in wastewater systems, Sci. Total Environ. 571 (2016) 643–657.

[5] Y. Yang, J.J. Pignatello, J. Ma, W.A. Mitch, Comparison of halide impacts on the efficiency of contaminant degradation by sulfate and hydroxyl radical-based advanced oxidation processes (AOPs), Environ. Sci. Technol. 48 (2014) 2344-2351.

[6] X. Lou, C. Fang, Z. Geng, Y. Jin, D. Xiao, Z. Wang, J. Liu, Y. Guo, Significantly enhanced base activation of PMS by polyphosphates: Kinetics and mechanism, Chemosphere 173 (2017) 529–534.

[7] G.P. Anipsitakis, D.D. Dionysiou, Degradation of organic contaminants in water with sulfate radicals generated by the conjunction of peroxymonosulfate with cobalt, Environ. Sci. Technol. 37 (20) (2003) 4790-4797.

[8] Y. Cao, W. Qiu, Y. Zhao, J. Li, Y. Yang, S.Y. Pang, G. Liu, The degradation of chloramphenicol by O_3/PMS and the impact of O_3-based AOPs pre-oxidation on dichloroacetamide generation in post-chlorination, Chem. Eng. J. 401 (2020) 126146.

[9] J. Li, M.J. Xu, G. Yao, B. Lai, Enhancement of the degradation of atrazine through $CoFe_2O_4$ activated peroxymonosulfate (PMS) process: kinetic, degradation intermediates, and toxicity evaluation, Chem. Eng. J. 348 (2018) 1012–1024.

[10] C. Qi, X. Liu, J. Ma, C. Lin, X. Li, H. Zhang, Activation of peroxymonosulfate by base: implications for the degradation of organic pollutants, Chemosphere 151 (2016) 280–288.

[11] J.R. Chueca, C. Amor, T. Silva, D.D. Dionysiou, G.I. Puma, M.S. Lucas, J.A. Peres, Treatment of winery wastewater by sulphate radicals: HSO_5^-/transition metal/UV-A LEDs, Chem. Eng. J. 310 (2017) 473–483.

[12] L. Wang, Q. Zhang, B. Chen, Y. Bu, Y. Chen, J. Ma, F. L. Ortiz, Photolysis and photocatalysis of halo-acetic acids in water: A review of kinetics, influencing factors, products, pathways, and mechanisms, J. Hazard. Mater. 391 (2020) 122143.

[13] L. Wang, X. Huang, M. Han, L. Lyu, T. Li, Y. Gao, Q. Zeng, C. Hu, Efficient inhibition of photogenerated electron-hole recombination through persulfate activation and dual-pathway degradation of micropollutants over iron molybdate, Appl. Catal. B Environ. 257 (2019) 117904.

[14] X. Zhou, Z. Zeng, G. Zeng, C. Lai, R. Xiao, S. Liu, D. Huang, L. Qin, B. Li, H. Yi, Y. Fu, L. Li, Z. Wang, Persulfate activation by swine bone char-derived hierarchical porous carbon: Multiple mechanism system for organic pollutant degradation in aqueous media, Chem. Eng. J. 383 (2020) 123091.

[15] F. Ghanbari, M. Moradi, Application of peroxymonosulfate and its activation methods for degradation of environmental organic pollutants, Chem. Eng. J. 310 (2017) 41-62.

[16] Y. Ding, X. Wang, L. Fu, X. Peng, C. Pan, Q. Mao, C. Wang, J. Yan, Nonradicals induced degradation of organic pollutants by peroxydisulfate (PDS) and peroxymonosulfate (PMS): Recent advances and perspective, Sci. Total Environ. (2020) 142794.

[17] P. Liang, C. Zhang, X. Duan, H. Sun, S. Liu, M.O. Tade, S. Wang, An insight into metal organic framework derived N-doped graphene for the oxidative degradation of persistent contaminants: formation mechanism and generation of singlet oxygen from peroxymonosulfate, Environ. Sci. Nano 4 (2017) 315-324.

[18] X. Cheng, H. Guo, Y. Zhang, X. Wu, Y. Liu, Non-photochemical production of singlet oxygen via activation of persulfate by carbon nanotubes, Water Res. 113 (2017) 80-88.

[19] X. Duan, C. Su, L. Zhou, H. Sun, A. Suvorova, T. Odedairo, Z. Zhu, Z. Shao, S. Wang, Surface controlled generation of reactive radicals from persulfate by carbocatalysis on nano-diamonds, Appl. Catal. B 194 (2016) 7-15.

[20] H. Lee, H.J. Lee, J. Jeong, J. Lee, N.B. Park, C. Lee, Activation of persulfates by carbon nanotubes: oxidation of organic compounds by nonradical mechanism, Chem. Eng. J. 266 (2015) 28-33.

[21] X. Chen, W.D. Oh, Z.T. Hu, Y.M. Sun, R.D. Webster, S.Z. Li, T.T. Lim, Enhancing sulfacetamide degradation by peroxymonosulfate activation with N-doped graphene produced through delicately-controlled nitrogen functionalization via tweaking thermal annealing processes, Appl. Catal. B 225 (2018) 243-257.

[22] H. Lee, H.J Lee, J. Jeong, J. Lee, N.B. Park, C. Lee, Activation of persulfates by carbon nanotubes: oxidation of organic compounds by nonradical mechanism, Chem. Eng. J. 266 (2015) 28-33.

[23] X. Zhou, Q. Zhao, J. Wang, Z. Chen, Z. Chen, Nonradical oxidation processes in PMS-based heterogeneous catalytic system: Generation, Identification, Oxidation characteristics, Challenges response and Application prospects, Chem. Eng. J. (2020) 128312.

[24] W.D. Oh, T.T. Lim, Design and application of heterogeneous catalysts as peroxydisulfate activator for organics removal: an overview, Chem. Eng. J. 358 (2019) 110-133.

[25] W. Peng, Y. Dong, Y. Fu, L. Wang, Q. Li, Y. Liu, Q. Fan, Z. Wang, Non-radical reactions in persulfate-based homogeneous degradation processes: A review, Chem. Eng. J. (2020) 127818.